

## The $\gamma$ -ray Emission of Star-Forming Galaxies

M. AJELLO,<sup>1</sup> M. DI MAURO,<sup>2,3</sup> V. S. PALIYA,<sup>4</sup> AND S. GARRAPPA<sup>4</sup>

<sup>1</sup>*Department of Physics and Astronomy, Clemson University, Kinard Lab of Physics, Clemson, SC 29634-0978, USA*

<sup>2</sup>*NASA Goddard Space Flight Center, Greenbelt, MD 20771, USA*

<sup>3</sup>*Catholic University of America, Department of Physics, Washington DC 20064, USA*

<sup>4</sup>*Deutsches Elektronen Synchrotron DESY, D-15738 Zeuthen, Germany*

### ABSTRACT

A majority of the  $\gamma$ -ray emission from star-forming galaxies is generated by the interaction of high-energy cosmic rays with the interstellar gas and radiation fields. Star-forming galaxies are expected to contribute to both the extragalactic  $\gamma$ -ray background and the IceCube astrophysical neutrino flux. Using roughly 10 years of  $\gamma$ -ray data taken by the *Fermi* Large Area Telescope, in this study we constrain the  $\gamma$ -ray properties of star-forming galaxies. We report the detection of 11 bona-fide  $\gamma$ -ray emitting galaxies and 2 candidates. Moreover, we show that the cumulative  $\gamma$ -ray emission of below-threshold galaxies is also significantly detected at  $\sim 5\sigma$  confidence. The  $\gamma$ -ray luminosity of resolved and unresolved galaxies is found to correlate with the total (8-1000  $\mu\text{m}$ ) infrared luminosity as previously determined. Above 1 GeV, the spectral energy distribution of resolved and unresolved galaxies is found to be compatible with a power law with a photon index of  $\approx 2.2 - 2.3$ . Finally, we find that star-forming galaxies account for roughly 5% and 3% of the extragalactic  $\gamma$ -ray background and the IceCube neutrino flux, respectively.

*Keywords:* galaxies: starburst – gamma rays: diffuse background –neutrinos

### 1. INTRODUCTION

The origin of the extragalactic  $\gamma$ -ray background (EGB) has been debated since its discovery by the OSO-3 satellite (Kraushaar et al. 1973). The EGB spectrum has been measured with good precision from 100 MeV to 820 GeV by the Large Area Telescope (LAT) on board of the *Fermi Gamma-Ray Space Telescope* (Ackermann et al. 2014) and has been ascribed

to the emission of resolved and unresolved point sources like blazars, star-forming and radio galaxies (Ajello et al. 2015; Di Mauro & Donato 2014). While the contribution of blazars to the EGB is reasonably well constrained and understood (see, e.g., Di Mauro et al. 2014; Ajello et al. 2015; Ackermann et al. 2016; Di Mauro et al. 2018), the contribution from star-forming and radio galaxies is not. Analyses that have estimated the contribution of star-forming and radio galaxies to the EGB were based on 7 and 12 detected sources, respectively (Ackermann et al. 2012a; Di Mauro et al. 2013), yielding considerable uncertainties.

majello@g.clemson.edu  
mdimauro@slac.stanford.edu  
vaidehi.s.paliya@gmail.com

Taking advantage of the increased sensitivity provided by ten year of LAT data, in this study we re-evaluate the  $\gamma$ -ray properties of star-forming galaxies (SFGs) whose  $\gamma$ -ray emission is partly of hadronic origin, being generated by cosmic-ray (CR) interactions with ambient gas and interstellar radiation fields. The detection of a flux of astrophysical neutrinos by IceCube (Aartsen et al. 2013; Aartsen et al. 2014; Aartsen et al. 2015) with TeV-PeV energies has renewed the interest in SFGs since the hadronic interactions that generate high-energy  $\gamma$  rays inevitably lead to the generation of high-energy neutrinos.

The lack of anisotropy in the IceCube signal and template analyses show that most ( $\gtrsim 86\%$ ) of the IceCube signal is likely of extragalactic origin (Aartsen et al. 2017a). Moreover, the absence of neutrino point-like sources and the non-detection of muon neutrino multiplets at  $> 50$  TeV imply that the population responsible for the majority of the IceCube neutrinos is produced by unresolved sources with a local density of  $\geq 10^{-8} \text{ Mpc}^{-3}$  or  $\geq 10^{-6} \text{ Mpc}^{-3}$  for evolving and non-evolving populations respectively (Ahlers & Halzen 2014; Murase & Waxman 2016; Peng & Wang 2017). Such populations could be jetted active galactic nuclei (blazars and/or radio galaxies) and star-forming galaxies. However, it seems unlikely that either of them can account for the totality of the IceCube neutrino flux. Indeed, while a neutrino event has been found in suggestive ( $\approx 3\sigma$ ) coincidence with a flaring blazar (IceCube Collaboration et al. 2018), cross-correlation studies of all the neutrino events and LAT blazars demonstrated that blazars can only produce a fraction  $\lesssim 27\%$  of the neutrino intensity above 10 TeV (Aartsen et al. 2017b). Similarly, the non-blazar fraction of the EGB at  $> 50$  GeV (Ackermann et al. 2016) limits the contribution of SFGs to the diffuse neutrino background to  $\lesssim 30\%$  (Bechtol et al. 2017).

In this paper we use roughly 10 years of *Fermi*-LAT data to study the global properties of SFGs and constrain their contribution to the EGB and IceCube astrophysical signal. This paper is organized as follows: § 2 and § 3 present the properties of the sample and method used for the analysis. The results for the properties of SFGs are presented in § 4, § 5, and § 6, and their contribution to the EGB and IceCube neutrino flux is discussed in § 7. Finally, § 8 summarizes the results. Throughout this paper, a standard concordance cosmology was assumed ( $H_0=71 \text{ km s}^{-1} \text{ Mpc}^{-1}$ ,  $\Omega_M=1-\Omega_\Lambda=0.27$ ).

## 2. SAMPLE OF GALAXIES

Massive star formation is fueled by dense molecular gas in the interstellar medium (ISM). In order to select a sample of galaxies with unambiguous ongoing star formation, we base our sample of galaxies on the following resources:

- The survey of HCN emission from 65 infrared (IR) galaxies published in Gao & Solomon (2004). This includes nine ultraluminous infrared galaxies, 22 luminous infrared galaxies, and 34 normal spiral galaxies with low IR luminosity.
- The sample of 83 nearby starburst galaxies with UV-to-FIR data selected based on the availability of UV data from the *International Ultraviolet (UV) Explorer* (Wu et al. 2002). This sample was also used in the previous *Fermi*-LAT analysis of SFGs (Ackermann et al. 2012a, hereafter ACK12).
- The *Infrared Astronomical Satellite* (IRAS) Revised Bright Galaxy Sample (RBGS). This is a complete flux-limited survey of all extragalactic objects with total 60 micron flux density greater than 5.24 Jy. This sample covers the entire sky surveyed by *IRAS* at Galactic latitude  $|b| > 5^\circ$ . The RBGS includes 629 objects, with

a median sample redshift of  $z = 0.0082$  and a maximum redshift of  $z = 0.0876$  (Sanders et al. 2003).

The selection of the above catalogs results in a sample of 683 SFGs with known position, redshift, distance, and infrared luminosity ( $L_{\text{IR}}$ ) in the wavelength range 8–1000  $\mu\text{m}$ .  $L_{\text{IR}}$  is derived by fitting a single temperature dust emissivity model to the flux reported in the 4 *IRAS* bands and should be accurate to  $\pm 5\%$  for dust temperatures in the 25–65 K range (see Sanders & Mirabel 1996, for details).

We then remove all blazars from our list based on positional coincidence with sources from the following two catalogs. First, we remove all sources that are positionally coincident with any of the associated point sources (other than associations with galaxies) from the preliminary *Fermi*-LAT 8-year point source list (FL8Y<sup>1</sup>). Additionally, we remove all sources that are positionally coincident with sources from the 5th edition of Roma-BZCAT (Massaro et al. 2015), which is one of the most up-to-date lists of blazars. These cuts reduce the number of SFGs in our sample to 588, which will be considered in the rest of our analysis.

In Figure 1 we show the distribution of the IR luminosity,  $L_{\text{IR}}$ , for our full sample of SFGs and the subset of galaxies used in ACK12. The peak of the distribution is around  $\text{Log}(L_{\text{IR}}/L_{\odot}) = 10 - 11$ , but the full sample contains many more galaxies with  $L_{\text{IR}} < 10^{10} L_{\odot}$  compared to the ACK12 subset.

### 3. FERMI-LAT DATA ANALYSIS

#### 3.1. Analysis of Individual Galaxies

We analyze the *Fermi*-LAT data for each source in our sample in order to determine

<sup>1</sup> This worked started well before the LAT 8-year source catalog (4FGL The *Fermi*-LAT collaboration 2019) became available. For the FL8Y see: <https://fermi.gsfc.nasa.gov/ssc/data/access/lat/fl8y>

whether or not it is detected (with a  $TS^2 > 25$ ). We analyze almost 10 years of Pass 8 data, from 2008 August 4 to 2018 March 4, selecting  $\gamma$ -ray events in the energy range  $E = [0.1, 800]$  GeV, passing the standard data quality selection criteria<sup>3</sup>. We consider events belonging to the Pass 8 SOURCE event class, and use the corresponding instrument response functions (IRFs) P8R3\_SOURCE\_V2, since we are interested in the detection and study of point sources.

We reduce the contamination from the low-energy Earth limb emission by applying a zenith angle cut to the data. Following the FL8Y<sup>4</sup> analysis, we make a harder cut at low energies by selecting event types with the best point spread function (PSF). For  $E = [0.1, 0.3]$  GeV, we select events belonging to the PSF2 and PSF3 classes with zenith angles  $< 90^\circ$ . For  $E = [0.3, 1.0]$  GeV we select PSF1, PSF2 and PSF3 event types with zenith angles  $< 100^\circ$ . And above 1 GeV we use all events (PSF0, PSF1, PSF2, PSF3) with zenith angles less than  $105^\circ$ . This choice reduces the contribution of the Earth limb contamination to less than 10% of the total background.

We employ an analysis pipeline based on *FermiPy*, which is a Python package, based on the *Fermi* Science Tools, that automates analyses (Wood et al. 2017)<sup>5</sup>. *FermiPy* includes tools that perform fits of the model to the  $\gamma$ -ray data, detect new point sources, calculate the source spectral energy distribution (SED), and

<sup>2</sup> The Test Statistic,  $TS$ , is defined as  $TS = 2(\log L_1 - \log L_0)$ , where  $\log L_1$  and  $\log L_0$  are the log-likelihood values for the case of background plus source and only background respectively (Mattox et al. 1996).

<sup>3</sup> We apply the filter ( $DATA\_QUAL > 0$ )&&(LAT\_CONFIG == 1) with the `gtmktime` tool of the Science Tools. See [https://fermi.gsfc.nasa.gov/ssc/data/analysis/scitools/binning\\_likelihood\\_tutorial.html](https://fermi.gsfc.nasa.gov/ssc/data/analysis/scitools/binning_likelihood_tutorial.html) for further details.

<sup>4</sup> [https://fermi.gsfc.nasa.gov/ssc/data/access/lat/fl8y/FL8Y\\_description.v5.pdf](https://fermi.gsfc.nasa.gov/ssc/data/access/lat/fl8y/FL8Y_description.v5.pdf)

<sup>5</sup> See <http://fermipy.readthedocs.io/en/latest/>.

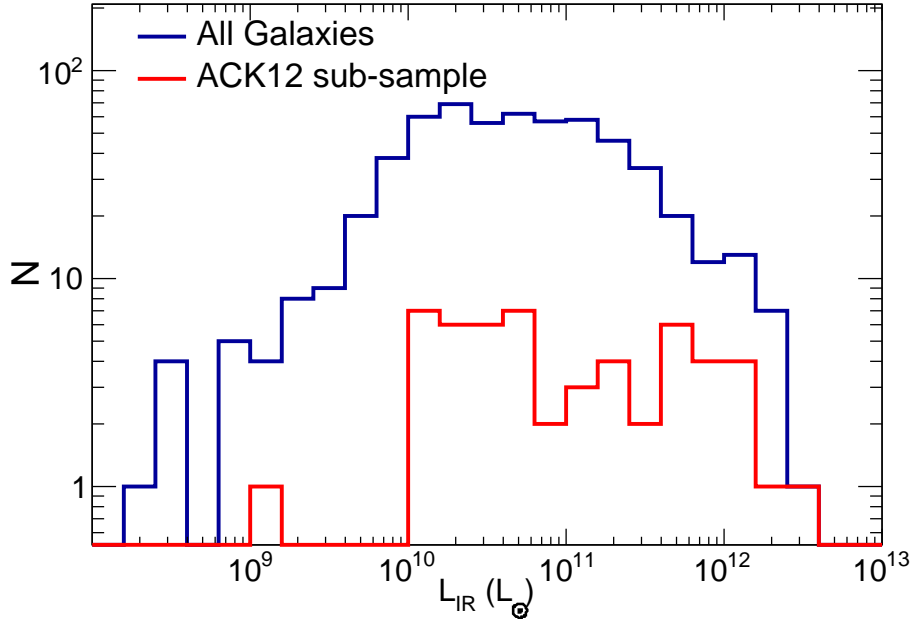


**Figure 1.** Distribution of infrared luminosity for the full sample of galaxies described in § 2 and the subset of objects of ACK12.

test for the presence of source extension and variability.

For each galaxy in our sample we consider a region of interest (ROI) of  $12^\circ \times 12^\circ$  centered at the respective galaxy, and each ROI is analyzed separately. In each ROI, we bin the data with a pixel size of  $0.06^\circ$  and 8 energy bins per decade. We model the Galactic diffuse emission using the interstellar emission model (IEM) released with Pass 8 data (`gll_iem_v06.fits`, Acero et al. 2016). Correspondingly, we use the standard template for the isotropic emission (`iso_P8R2_SOURCE_V6_v06.txt`)<sup>6</sup>. Two objects, the Large and the Small Magellanic clouds (LMC and SMC), are modeled as spatially extended sources adopting the templates used in the FL8Y (see App. A). The point sources are modeled using the FL8Y catalog. Energy dispersion is applied to all sources in the

<sup>6</sup> For descriptions of these templates, see <http://fermi.gsfc.nasa.gov/ssc/data/access/lat/BackgroundModels.html>.

model except the isotropic template<sup>7</sup>. This includes the Galactic diffuse templates. We used the implementation of the energy dispersion present in the Fermi tools<sup>8</sup>. Specifically we have fixed `apply_edisp=True` and `edisp_bins=-1`.

During the optimization of each ROI, we first relocalize the source of interest. We then search for new point sources with  $TS > 25$ , which are inserted in the model. These sources are found generating a  $TS$  map where a test source is moved across the ROI. After this first step we test whether the emission of the SFG candidate is consistent with that of a point-like or spatially extended source. Out of the 588 galaxies searched in this way, 13 SFGs are de-

<sup>7</sup> The isotropic template, which has been derived from observed data, includes already the effect of energy dispersion and does not need to be corrected.

<sup>8</sup> For more information see [https://fermi.gsfc.nasa.gov/ssc/data/analysis/documentation/Pass8\\_edisp\\_usage.html](https://fermi.gsfc.nasa.gov/ssc/data/analysis/documentation/Pass8_edisp_usage.html)

tected with significance<sup>9</sup>  $> 4.6\sigma$  ( $TS > 25$ ). Another galaxy (UGC 11041) is also detected but we later show that its emission is likely due to a relativistic jet. Properties of the detected galaxies, including the SEDs and lightcurves, are described in § 4.

### 3.2. Stacking Analysis of Unresolved Galaxies

Here we test whether the LAT detects the collective emission from galaxies too faint to be detected individually. We use the sample of 575 undetected objects from the previous section. A pre-analysis is performed similar to the analysis of detected objects (see Section 3.1) with a few key differences. First, we select photons of all PSF types (0,1,2, and 3) from 0.1 GeV to 800 GeV within  $15^\circ$  of the galaxy of interest to properly model the background. Similarly to § 3.1, background sources include those in the FL8Y source list plus any new source detected here with a  $TS > 25$ . These sources are found with an iterative procedure generating a  $TS$  map and looking for excesses above the  $TS > 25$  threshold. In order to retain sensitivity to a range of power-law spectral slopes,  $TS$  maps are generated for photon indices of 2.0, 2.5, and 3.0. Once all excesses above background have been inserted in the background model a final fit is performed to optimize all the free parameters (those of the diffuse templates and background sources) in the ROI.

In order to detect the collective emission of the undetected galaxies, we perform a stacking analysis where we sum the log-likelihood profiles generated for the spectral parameters of the SFGs under the assumption that the source population can be characterized by some average quantities (i.e., spectral index and flux), as described in the next section. In generating the log-likelihood profiles the parameters of the

isotropic and Galactic diffuse templates are left free to vary, while all those of the background sources are kept fixed at their optimized values. Further details on the stacking are also reported in Paliya et al. (2019).

## 4. DETECTION OF INDIVIDUAL AND UNRESOLVED GALAXIES

### 4.1. Individual Galaxies

From our analysis we detect significant  $\gamma$ -ray emission ( $TS > 25$ ) at the positions of 13 SFGs, whose characteristics are reported in Table 1. Our sample of detected galaxies contains the seven already reported in ACK12 (LMC, SMC, M31, M82, NGC 253, NGC 4945 and NGC 1068). In addition to those, NGC 2146 and Arp 220 (reported already by Tang et al. 2014; Peng et al. 2016) are also detected in this work. Gamma-ray emission from NGC 2403 and NGC 3424 has also been previously reported by Linden (2017), who, however, flagged them as potential background fluctuations. Finally, our analysis reports the first detection of emission from M33<sup>10</sup> and Arp 299. Note that we also detect significant ( $TS = 44$ )  $\gamma$ -ray emission from UGC 11041, but due to its strong variability (see Table 2 and App. A.0.3), this emission is likely not associated to star-formation processes but to a jet. Therefore UGC 11041 is not part of our sample of detected galaxies.

M33, also known as the Triangulum galaxy, at a distance of 870 kpc, is the smallest spiral galaxy in the Local Group. Its star-formation rate (SFR) is in the range  $0.26\text{--}0.70 M_\odot \text{ yr}^{-1}$  (Gardan et al. 2007).

Arp 299 at  $\sim 48 \text{ Mpc}$ , is much more distant than M33 and it is an interacting system, at an early dynamical stage, composed of two individual galaxies. Powerful starburst regions with

<sup>9</sup> The conversion between  $TS$  and  $\sigma$  was performed using a  $\chi^2$  distribution with 2 degrees of freedom, corresponding to the two free spectral parameters.

<sup>10</sup> We note that a source is detected at the position of M33 also in FL8Y. However, such source is not present in 4FGL possibly due to the updated diffuse model. Its effect will be studied in a future publication.

**Table 1.** List of SFGs detected in our analysis. In this table, we report name, coordinates, distance from Earth, IR luminosity,  $TS$ ,  $\gamma$ -ray energy flux and luminosity of each source. The table is divided into two blocks. The upper block lists the bona fide sample, while the lower block reports the SFGs that are offset with respect to the IR- $\gamma$ -ray luminosity correlation.

Name	R.A. (J2000) [deg]	Decl. (J2000) [deg]	dist. <sup>a</sup> [Mpc]	$\log_{10} L_{\text{IR}}^{8-1000\mu\text{m}}$ [ $L_{\odot}$ ]	$TS$	$S^b$	$\log_{10} L_{\gamma}$ [ $\text{erg s}^{-1}$ ]
M31	10.69	41.27	0.78	9.39	122	$0.63 \pm 0.07$	38.66
NGC 253	11.89	-25.28	3.30	10.44	608	$0.89 \pm 0.07$	40.05
SMC	13.18	-72.83	0.063	7.86	1938	$2.90 \pm 0.12$	37.14
M33	23.47	30.67	0.85	9.07	41	$0.21 \pm 0.04$	38.25
NGC 1068	40.68	-0.01	10.1	11.27	335	$0.68 \pm 0.05$	40.92
LMC	80.89	-69.76	0.05	8.82	4797	$10.7 \pm 0.3$	37.50
NGC 2146	94.66	78.36	18.0	11.07	73	$0.23 \pm 0.04$	40.95
M82	148.97	69.68	3.70	10.77	1186	$1.13 \pm 0.05$	40.27
Arp 299	172.13	58.57	47.7	11.88	32	$0.13 \pm 0.04$	41.55
NGC 4945	196.36	-49.47	3.80	10.48	489	$1.15 \pm 0.07$	40.30
Arp 220	233.74	23.51	79.9	12.21	84	$0.35 \pm 0.05$	42.42
NGC 2403	114.22	65.61	3.2	9.19	49	$0.17 \pm 0.04$	39.33
NGC 3424	162.94	32.90	27.2	10.30	40	$0.17 \pm 0.05$	41.18

<sup>a</sup>Distances are from: ACK12 for the Local Group galaxies (M31, SMC, M33, and LMC), [Mouhcine et al. \(2005\)](#) for NGC 253, [Nasonova et al. \(2011\)](#) for NGC 1068, [Adamo et al. \(2012\)](#) for NGC 2146, [Vacca et al. \(2015\)](#) for M82, the redshift for Arp 229 and Arp 220, [Mould & Sakai \(2008\)](#) for NGC 4945, [Tully et al. \(2013\)](#) for NGC 2403, and [Theureau et al. \(2007\)](#) for NGC 3424. IR luminosities are taken from [Wu et al. \(2002\)](#), [Sanders et al. \(2003\)](#), and [Gao & Solomon \(2004\)](#).

<sup>b</sup> $\gamma$ -ray flux in units of  $10^{-11} \text{ erg cm}^{-2} \text{ s}^{-1}$ .

SFRs of about  $100 M_{\odot} \text{ yr}^{-1}$  have been identified there by [Alonso-Herrero et al. \(2000\)](#). We consider all  $\gamma$ -ray sources except NGC 3424 and NGC 2403 as part of our bona-fide sample of galaxies. These two galaxies will be discussed in more detail in § 5.1.1.

We test whether the  $\gamma$ -ray spectra of the detected SFGs are described better by a power law (PL) or a log-parabola (LP). These SED shapes are defined as follows:

$$\frac{dN}{dE} = K \left( \frac{E}{E_0} \right)^{-\Gamma}, \quad (1)$$

for the PL, where  $K$  is the normalization,  $E_0$  is fixed to 1 GeV, and  $\Gamma$  is the spectral index;

$$\frac{dN}{dE} = K \left( \frac{E}{E_0} \right)^{-\Gamma + \beta \log(E/E_0)}, \quad (2)$$

for the LP, where  $\beta$  is the curvature index. In order to choose between the above models we compute the  $TS$  of curvature ( $TS_{\text{curv}}$ ) defined as  $TS_{\text{curv}} = -2(\log L_{\text{PL}} - \log L_{\text{LP}})$ . Only two galaxies, the LMC and the SMC, have a significant ( $TS_{\text{curv}} > 25$ , i.e.  $>5\sigma$ ) curvature. The SED parameters of all these detected galaxies are reported in Table 2, while their SEDs are plotted in Figures 2 and 3.

Finally, we extract a light curve for each galaxy using the tools available in `Fermipy`. This is done by dividing the entire dataset into time intervals of one-month duration for the six brightest sources and 3 month duration for the rest. Having more bins increases the ability to detect variability for bright sources. On the other hand, for fainter sources one-month time bins are too narrow to allow detection of the source in most bins. For each time interval a fit of the model to the data is performed, from which we obtain the flux, SED, and detection  $TS$ . In the final step the  $TS$  for the variability ( $TS_{\text{var}}$ , see Appendix A.0.3) is calculated following Nolan et al. (2012). Since, different time bins are used for different sources, we report in Table 2 the values of the significance of variability  $\sigma_{\text{var}}$ , computed considering that there are 119 time bins and 118 degrees of freedom for the first six bright galaxies and 39 time bins and 38 degrees of freedom for the rest.

As already mentioned, UGC 11041 is the only galaxy with a significant variability ( $5.7\sigma_{\text{var}}$ ). Moreover, this source underwent a strong flare between MJD 56600 and 56800, as can be observed from its lightcurve (see App. A). This flare, together with the spatial coincidence of the galaxy with a radio source in the NVSS catalog, suggests that the observed  $\gamma$ -ray emission is due to a relativistic jet, as opposed to star-formation activity. This source is thus excluded from further analysis. The lightcurves of all the galaxies that we detected are shown in the Appendix § A.0.3.

#### 4.2. Unresolved Galaxies

For each undetected galaxy, whose spectrum is modeled with a power law, we generate a bi-dimensional log-likelihood profile varying its photon index and photon flux (measured in the 100 MeV – 800 GeV energy range). By subtracting the log-likelihood of the null hypothesis ( $\log L_{\text{null}}$ ), i.e., the likelihood of the data if the galaxy in question is not a gamma-ray emitter,

we define the  $TS = 2(\log L - \log L_{\text{null}})$ . We sum the  $TS$  profiles of every galaxy to quantify the significance of their collective detection, assuming that the entire population can be characterized by an average photon index and an average flux. Figure 4 shows the results of this stacking analysis for the entire sample of undetected galaxies (574, left) and the sub-sample of undetected galaxies reported in Ackermann et al. (2012a) (56, right).

Figure 4 illustrates that the average emission from all unresolved galaxies is detected by the LAT with a  $TS=23$  (corresponding to  $\sim 4.4\sigma$ ). The average  $\gamma$ -ray emission of the ACK12 sub-sample is detected with  $TS=30$  ( $\sim 5.1\sigma$ ). The signal is stronger for the ACK12 sub-sample compared to the entire sample (which is  $> 10$  times larger in number) because the galaxies in ACK12 are distributed over a narrower range of bright IR luminosities and fluxes (see Figure 1). The average photon index for the two sets is  $\Gamma = 2.21 \pm 0.12$  and  $\Gamma = 2.00 \pm 0.12$ , respectively. The average  $\gamma$ -ray spectrum of unresolved SFGs is thus as hard as the typical spectrum of starburst galaxies with  $L_{\text{IR}} = 10^{11-12} L_{\odot}$  (see Table 2 and Ackermann et al. 2012a).

## 5. THE $L_{\gamma}$ - $L_{\text{IR}}$ CORRELATION

### 5.1. Individual Galaxies

As already shown in Ackermann et al. (2012a), for SFGs a correlation exists between the  $\gamma$ -ray luminosity and the total IR luminosity, since both quantities are related to star-formation activity. Figure 5 shows the relation between  $\gamma$ -ray and IR luminosities for the objects detected in this work. NGC 2403 and NGC 3424 have an offset with respect to the general trend of all other SFGs: i.e., they are brighter in  $\gamma$  rays for a given IR luminosity. Therefore, we decide to select LMC, SMC, M82, NGC 253, NGC 4945, NGC 1068, M31, NGC 2146, M33, Arp 220, and Arp 299 as bona fide sources (i.e., galax-

Name	$TS_{\text{curv}}$	$\Gamma$	$\beta$	$E_0$ [GeV]	$\sigma_{\text{var}}$
LMC	335	1.42±0.05	-0.42±0.04	2.60±0.35	1.4
SMC	65	1.73±0.06	-0.10±0.03	1.25±0.18	2.9
M82	13	2.14±0.06			2.0
NGC 253	13	2.10±0.06			1.1
NGC 4945	2.3	2.22±0.07			1.1
NGC 1068	0.0	2.27±0.09			0.1
M31	6.0	2.23±0.11			0.7
Arp 220	1.3	2.48±0.14			0.0
M33	0.4	2.41±0.16			0.5
NGC 2146	1.3	2.27±0.07			0.9
Arp 299	0.1	2.11±0.19			0.1
NGC 2403	0.0	1.94±0.19			0.7
NGC 3424	2.5	1.97±0.20			0.7
UGC 11041	6.9	2.53±0.22			5.7

**Table 2.** SED parameters and significance of variability ( $\sigma_{\text{var}}$ ) for the SFGs detected in our analysis. We report the  $TS$  for the curvature ( $TS_{\text{curv}}$ ) and the SED parameters for the power-law model if  $TS_{\text{curv}} < 25$  and for the logparabola model if  $TS_{\text{curv}} \geq 25$ . The last column reports the significance of variability ( $\sigma_{\text{var}}$ , see the text and Appendix for further details).

ies whose  $\gamma$ -ray emission can be confidently attributed to star formation activity).

We fit a linear function (in log space) to the  $\gamma$ -ray and IR luminosities, for this bona fide sample. This gives values of  $\alpha = 1.27 \pm 0.03$  and  $\beta = 39.38 \pm 0.03$ , where the function being fit is defined as:

$$\log_{10} \left( \frac{L_{\gamma}}{\text{erg/s}} \right) = \beta + \alpha \log_{10} \left( \frac{L_{\text{IR}}}{10^{10} L_{\odot}} \right). \quad (3)$$

However, the fit results in a poor reduced chi-square  $\chi^2/d.o.f = 175/11$ . This is likely due to uncertainties in the distance of these galaxies and scatter in their  $\gamma$ -ray and IR properties. Indeed, within 100 Mpc, the typical distance is uncertain by  $\sim 10$ -20% (Freedman et al. 2001). The total IR luminosity ( $L_{\text{IR}}$ ) is also only accurate within 5% (Sanders & Mirabel 1996). Finally, for dust-poor systems,  $L_{\text{IR}}$  is not a reliable tracer of star formation (see e.g., Hayashida et al. 2013). It is therefore not very surprising to find such scatter in the  $L_{\gamma} - L_{\text{IR}}$  relation.

Although quantifying these uncertainties is difficult, if we assume a systematic uncertainty of 40% due to these effects, then the reduced  $\chi^2$  would be close to unity. We adopt this uncertainty for all further calculations.

In order to improve the fit quality, we incorporate the above effects as a source of systematic uncertainty in the  $\gamma$ -ray luminosity for each SFG in such a way that the reduced  $\chi^2$  ( $\chi^2/d.o.f.$ ) is of the order unity. We repeat the fit including this systematic uncertainty and obtain best-fit values for  $\alpha$  and  $\beta$  of:  $\alpha = 1.27 \pm 0.06$  and  $\beta = 39.47 \pm 0.08$ . In Figure 5 we show that the correlation derived here is similar to the one derived in Ackermann et al. (2012a). Moreover, we also measure a dispersion of 0.30 for the residuals of  $L_{\gamma}$  about the best fit, in agreement with Ackermann et al. (2012a) and Linden (2017).

If we perform a fit to all the SFGs detected in our analysis, thus adding also the sources which have an offset with respect to the IR- $\gamma$ -ray lu-



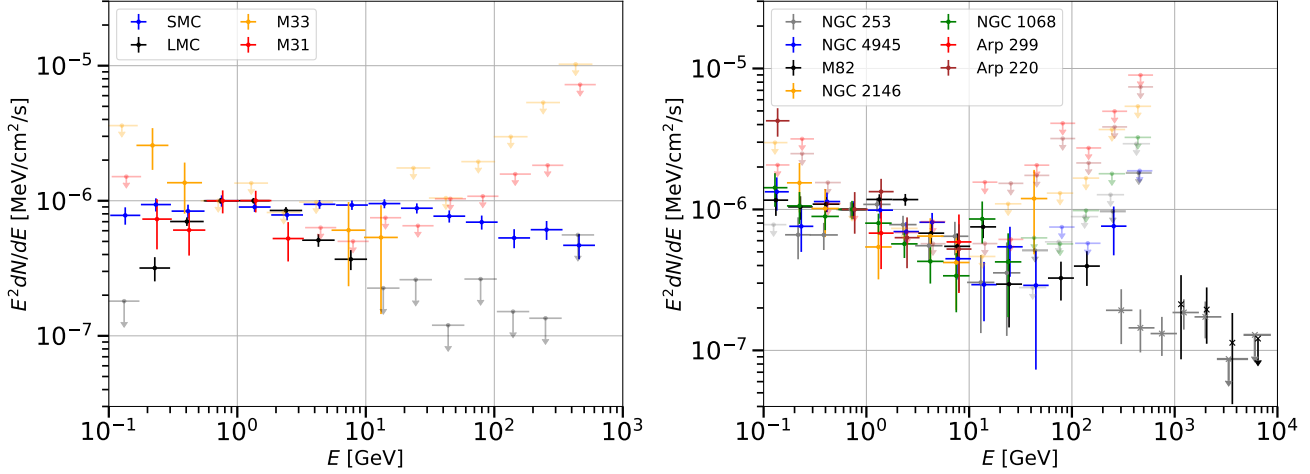


**Figure 2.** SEDs of bona fide SFGs. The galaxies have been ordered by increasing IR luminosity. Left Panel: SEDs for SMC, LMC, M33, and M31. Right Panel: NGC 253, NGC 4945, M82, NGC 2146, NGC 1068, Arp 299, and Arp 220. For NGC 253 and M82 we have included the SEDs measured by H.E.S.S. (Abdalla et al. 2018) and VERITAS (VERITAS Collaboration et al. 2009) (crosses), respectively. Upper limits (for  $TS < 6$ ) are plotted with lighter colors for visualization purposes.

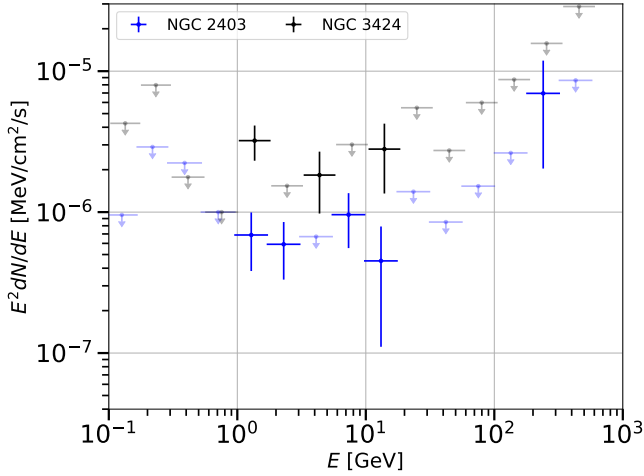


**Figure 3.** SEDs for candidate SFGs: NGC 2403 and NGC 3424. Upper limits (for  $TS < 6$ ) are plotted with lighter colors for visualization purposes.

minosity correlation, we find  $\alpha = 1.23 \pm 0.06$  and  $\beta = 39.55 \pm 0.07$ . This result is compatible with the one derived using the bona fide sample within uncertainties.

We test the significance of the correlation by performing a modified Kendall  $\tau$  rank correlation test (Akritas & Siebert 1996). This is a *survival analysis*, which can be used for the analysis of partially censored data sets containing

both detections and upper limits. The parameter  $\tau$  of the Kendall test varies between  $[-1, +1]$  for negative and positive correlation. We apply this test to our set of bona fide SFGs finding a value of  $\tau = 0.92$ . When also including NGC 2403 and NGC 3423 the value becomes  $\tau = 0.80$ . In order to convert this value into a significance we run Monte Carlo realizations of samples of 11 and 13 SFGs with no correlations. In particular we randomly draw  $\gamma$ -ray and IR luminosities in a range  $\log_{10} L_{\gamma} \in [37, 42]$  and  $\log_{10} L_{\text{IR}}[L_{\odot}] \in [7.5, 12]$ , respectively. For each realization we calculate the Kendall  $\tau$  parameter. In Figure 6 we show the histogram of the  $\tau$  values found for the  $30 \times 10^6$  realizations considered. As expected this is peaked at  $\tau \approx 0$  since the simulations are based on the absence of any correlation. We use this histogram to find the probability distribution function for the null hypothesis for the correlation and to find the p-value and significance associated to the  $\tau$  values reported above. The value of  $\tau = 0.92$  found for the bona fide sample is associated to a p-value of  $4.0 \times 10^{-7}$  and a significance of  $4.9 \sigma$ . On the other hand, the value of  $\tau = 0.80$  found with all detected SFGs is associated to a p-value

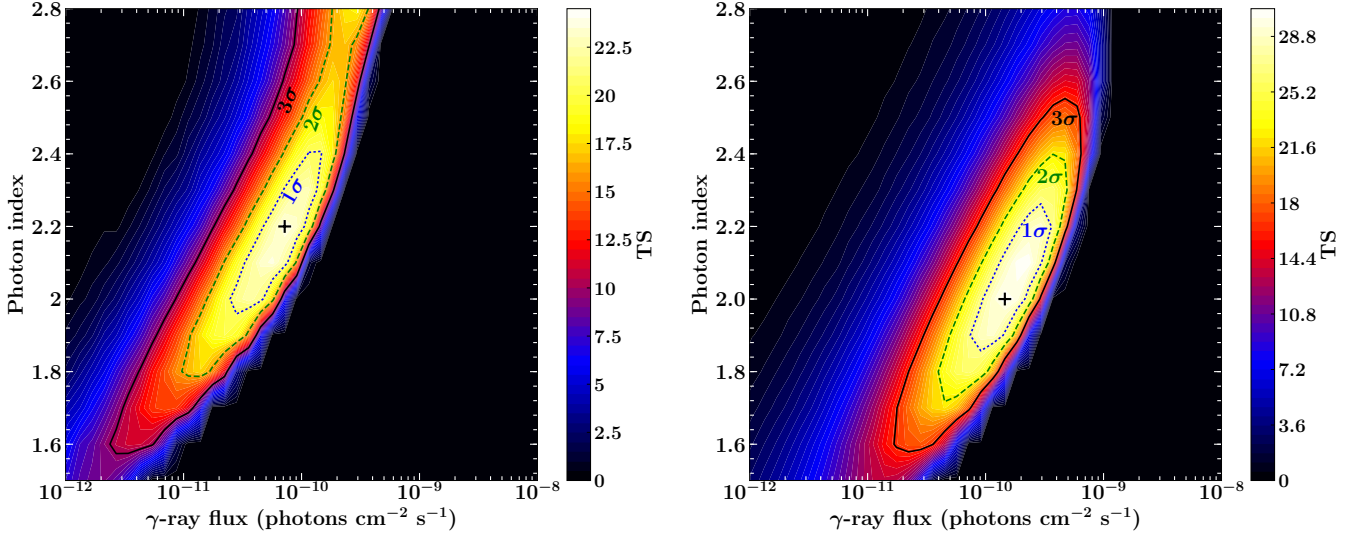


**Figure 4.** Detection significance as a function of photon index and  $\gamma$ -ray flux for the full sample of 574 undetected galaxies (left) and for the 56 undetected galaxies (right) in ACK12 sub-sample.

of  $6.7 \times 10^{-5}$  and a significance of  $3.8\sigma$ . As a comparison Ackermann et al. (2012a) found a p-value of 0.001. Therefore, the significance of the correlation between  $\gamma$ -ray and IR luminosities has grown significantly.

#### 5.1.1. Outliers

As reported above, NGC 2403 and NGC 3424 seem to be outliers in the  $L_\gamma - L_{\text{IR}}$  correlation. These objects (particularly NGC 3424) are also somewhat above the calorimetric limit<sup>11</sup> of Ackermann et al. (2012a), suggesting caution in interpreting the observed signal as due entirely to star formation activity. Indeed, these could be background fluctuations, background objects, or sources whose  $\gamma$ -ray emission may be partially due to processes other than star formation. The lack of variability and of strong radio emission disfavors the hypothesis of a strong relativistic jet. Among the two systems, only NGC 3424 is known to host a radio-quiet active galactic nucleus (AGN, Gavazzi et al. 2011); however the  $\gamma$ -ray emission from radio-quiet AGN remains to be detected (Ackermann et al. 2012b).

<sup>11</sup> A galaxy becomes a CR calorimeter when CRs deposit most of their energy within the galaxy itself.

We also note that NGC 3424 and NGC 2403 were analyzed in Peng et al. (2019) and Xi et al. (2020), where evidence of variability for both have been reported.

As discussed in the previous section, the correlation between IR and  $\gamma$ -ray luminosities is not modified significantly when these two objects are included in the analysis. Indeed, the values of  $\alpha$  and  $\beta$  found in this case are compatible within  $1\sigma$  with those derived using the bona fide sources (see Table 3). Thus, while the origin of the  $\gamma$ -ray emission of these two objects may remain unclear, their inclusion in the analysis changes the results negligibly.

## 5.2. $L_{\text{IR}}-L_\gamma$ Correlation with the Stacking Analysis

Here we test whether the  $\gamma$ -ray emission of unresolved galaxies is correlated with the IR emission in a way similar to what found in § 5.1 for the detected galaxies. In order to do this, for every unresolved galaxy in our sample we generate a three-dimensional log-likelihood profile as a function of the photon index ( $\Gamma$ ) and the two parameters ( $\alpha$  and  $\beta$ ) of the  $L_{\text{IR}}-L_\gamma$  correlation. By subtracting the log-likelihoods of

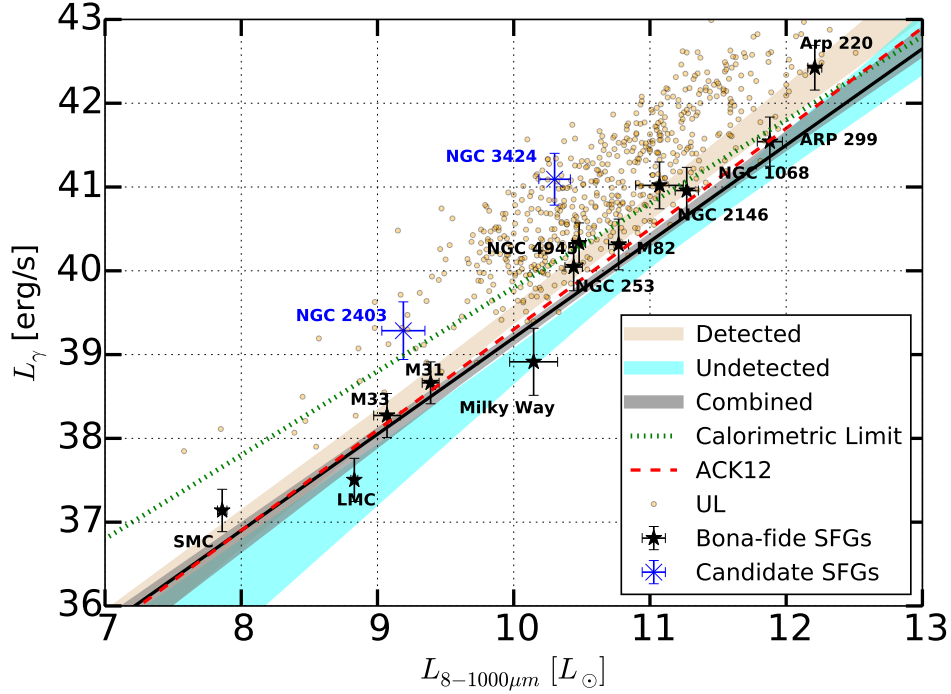


**Figure 5.** Gamma-ray vs. IR luminosities for the SFGs in our sample best fit. Bona fide SFGs are reported with black data points while galaxy candidates are shown with blue points. The best-fit  $1\sigma$  uncertainty band for the linear function in log space of the bona-fide sample is shown with a brown band, while the cyan band displays the  $1\sigma$  uncertainty band of the unresolved sources. The combined fit and its  $1\sigma$  uncertainty are plotted with the black line and the gray band, respectively. For comparison the red dashed line shows the best-fit correlation published in Ackermann et al. (2012a). The brown data points show  $\gamma$ -ray luminosity upper limits for all the individual galaxies in our sample, which are undetected in our analysis ( $TS < 25$ ).

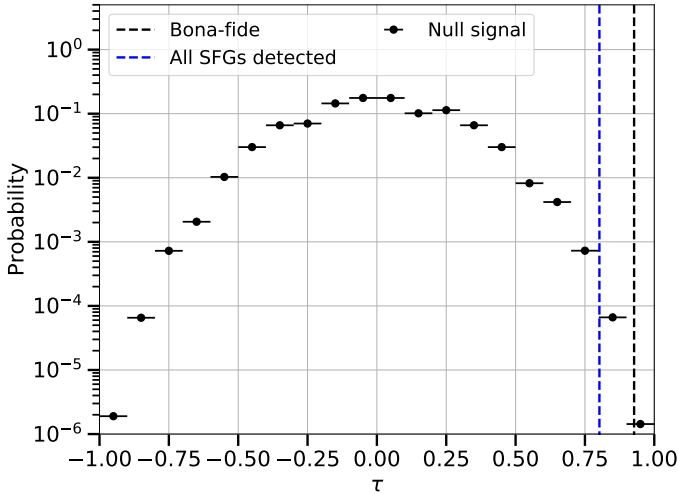


**Figure 6.** Probability distribution for the  $\tau$  parameter of the Kendall test performed with  $30 \times 10^6$  realizations (black data). We display with a black (blue) dashed line the  $\tau$  value found for the bona fide (complete) sample of detected sources.

the null hypotheses (i.e., there is no source) we transform these into  $TS$  profiles.

The results for the full sample of 574 galaxies and the ACK12 sub-sample are reported in Figure 7. In both cases the  $TS$  has grown substantially with respect to the photon-index/flux stacking, indicating that the 3-parameter fitting is better than the 2-parameter fitting. For the full sample and the ACK12 sample the  $TS$  values are now 60 ( $7.2\sigma$ ) and 45 ( $6.12\sigma$ ), respectively. The best-fit parameters,  $\alpha$  and  $\beta$ , are in very good agreement with those derived for detected galaxies (see Table 3). We thus conclude that the  $\gamma$ -ray luminosity of unresolved SFGs correlates with their IR luminosity.

### 5.3. Combined Constraints

The constraints on the  $\alpha$  and  $\beta$  parameters of Eq. 3 from resolved and unresolved sources

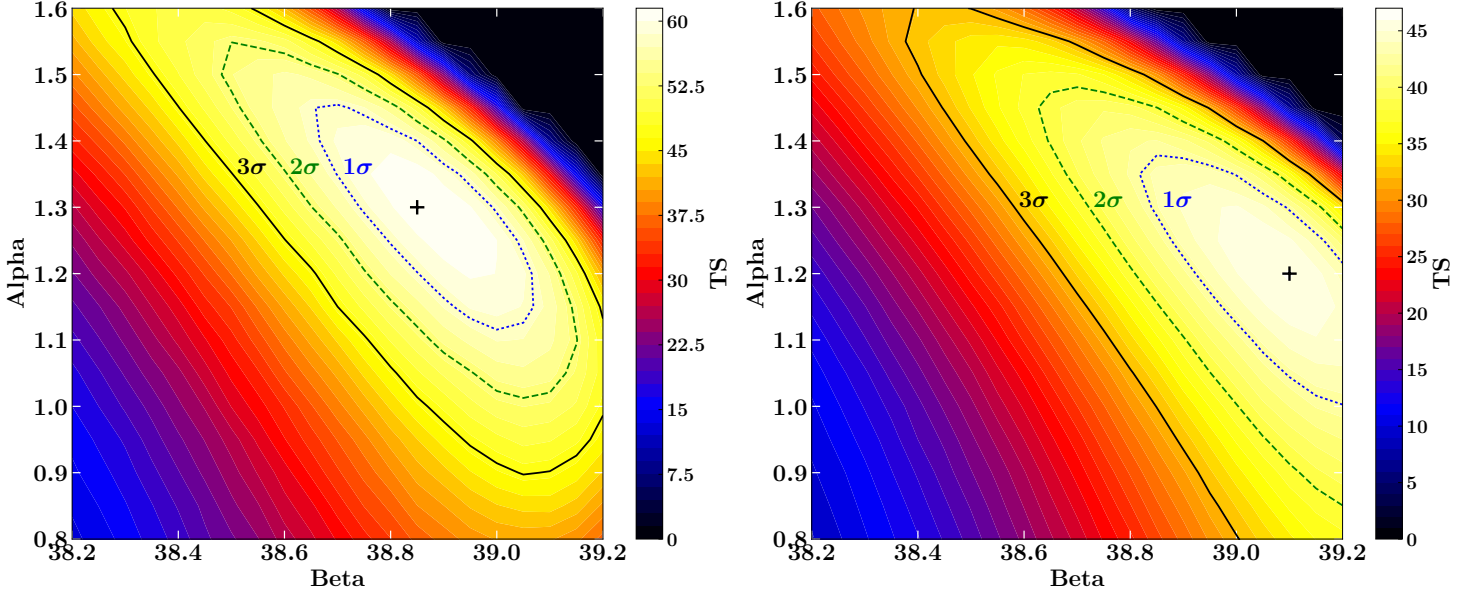


**Figure 7.** Detection significance as a function of photon index and  $\gamma$ -ray flux for all 574 undetected galaxies (left) and for the 56 undetected galaxies in the Ackermann et al. (2012a) sub-sample.

**Table 3.** Best-fit Parameters of the  $L_{\text{IR}}\text{-}L_{\gamma}$  Correlation

Sample	# Galaxies	$\alpha$	$\beta$
Detected (bona fide)	11	$1.27^{+0.06}_{-0.06}$	$39.47^{+0.08}_{-0.08}$
Detected (all)	13	$1.23^{+0.06}_{-0.06}$	$39.55^{+0.07}_{-0.07}$
Unresolved	574	$1.30^{+0.10}_{-0.10}$	$38.85^{+0.15}_{-0.11}$
Unresolved (ACK12)	56	$1.20^{+0.10}_{-0.15}$	$39.10^{+0.10}_{-0.10}$
Detected + Unresolved	587	$1.15^{+0.08}_{-0.03}$	$39.20^{+0.06}_{-0.05}$

can be combined to obtain a correlation that describes both populations. This is done by transforming the  $\chi^2$  of the fit described in § 5.1 for resolved objects into a log-likelihood as  $\frac{1}{2}\chi^2 = -\log L$ . This can be summed with the log-likelihood profile derived for unresolved galaxies, yielding best-fit parameters of  $\alpha = 1.15^{+0.08}_{-0.03}$  and  $\beta = 39.20^{+0.06}_{-0.05}$ .

## 6. THE $\gamma$ -RAY SPECTRAL ENERGY DISTRIBUTION OF GALAXIES

In this section we aim to understand whether SFGs have a common SED in the  $\gamma$ -ray band.

### 6.1. Combined SED of individually detected SFGs

One of the final goals of this work is to determine the contribution from SFGs to the EGB and to the astrophysical neutrino flux measured by IceCube. One key ingredient for this estimate is the SED of SFGs. Therefore, we consider the detected SFGs and perform a combined likelihood fit to their SEDs.

We consider a smoothly broken power-law (SBPL) model given by:

$$\frac{dN}{dE} = K \left( \frac{E}{E_0} \right)^{-\Gamma_1} \left( 1 + \left( \frac{E}{E_0} \right)^{-\Gamma_1 + \Gamma_2} \right)^{-\beta}, \quad (4)$$

where  $E_0$  is left as a free parameter. In this analysis, the normalization  $K$  is free to vary in the fitting for the galaxies SED, but all other parameters are common to all objects. The combined analysis is done by considering the SED results in the form of likelihood profiles as a function of  $dN/dE$  in each energy bin and combining them for all the sources of the bona fide sample except the SMC and the LMC. These two galaxies are removed from this analysis be-

cause they have the lowest IR luminosity, but the highest  $TS$  and would drive the result of the likelihood analysis. In the fit we also include, to best characterize the high-energy SED of SFGs, the TeV data points of NGC 253 detected by H.E.S.S. (Aharonian et al. 2005) and M82 detected by VERITAS (VERITAS Collaboration et al. 2009).

The best-fit values for the SED parameters are:  $\Gamma_1 = 2.28 \pm 0.07$ ,  $\Gamma_2 = 1.60 \pm 0.2$ ,  $\log_{10} E_0[\text{GeV}] = -0.50 \pm 0.15$  and  $\beta = 0.75 \pm 0.20$ . The values of the SED parameters do not change significantly if we exclude M31 and M33. The left panel of figure 8 shows the composite SED model (with its uncertainty) together with the SEDs of all detected galaxies scaled to a common value at 1 GeV. We find that other SED shapes, like PL or LP, are disfavored over the SBPL at the  $4.6\sigma$  and  $3.1\sigma$  level, respectively.

### 6.2. Combined SED of Unresolved Galaxies

The results of § 4.2 show that above  $>100$  MeV the spectrum of unresolved galaxies is hard, displaying a power-law index of  $\Gamma \approx 2.1 - 2.3$ . However, the true SED of SFGs may be more complex than a single power law and a hard power-law index may artificially originate when fitting around the SED peak. Moreover, a hard  $\gamma$ -ray spectrum could have interesting implications for the EGB and the neutrino background.

In order to test the shape of the SED of unresolved galaxies, we repeat the stacking analysis in two separate energy ranges: 0.1–1.0 GeV and 1.0–800 GeV and display the results in Figure 9. The lower energy range yields a  $TS \approx 0$ , which is translated into a 95% confidence level upper limit (see Figure 9). The energy range above 1 GeV confirms the results shown in § 4.2. In particular, the best-fit photon index is  $2.26^{+0.28}_{-0.16}$ . The  $TS$  is larger because the less-intense background and smaller PSF at these energies contribute to increase the signal-to-noise ratio. The analysis presented in this section shows that

the average SED of SFGs does not break above 1 GeV and remains compatible with a power law with  $\Gamma \approx 2.3$ . This is compatible with the SED found in Sec. 6.1 for the detected galaxies.

The right panel of Figure 8 shows the SED of unresolved galaxies, derived from the stacking analysis, compared to that of NGC 253 (Abdalla et al. 2018) and the composite SED model of § 6.1. Both models are good representations of the SED of unresolved SFGs and show that above 1 GeV the SED of galaxies (both resolved and unresolved) is compatible with a power law with a photon index  $\Gamma \sim 2.3$ . However, Figure 8 shows that our fit provides a better representation for the SED of detected galaxies than the model of Abdalla et al. (2018) and as such is adopted here. In the next section we use the composite SED model of detected SFGs as the representative shape for the SED of all SFGs, in order to predict their contribution to the EGB and IceCube astrophysical neutrino flux (Aartsen et al. 2014).

## 7. IMPLICATIONS FOR THE EGB AND ICECUBE NEUTRINO BACKGROUND

The EGB certainly contains the emission of SFGs. In the previous sections, we have reported the detection of a 11 SFGs and the emission from unresolved galaxies. Here we calculate the contribution of this source population to the *Fermi*-LAT EGB (Ackermann et al. 2014) and to the IceCube astrophysical neutrino flux (Aartsen et al. 2014).

The diffuse  $\gamma$ -ray flux due to the whole population of SFGs can be evaluated as follows:

$$\frac{d^2 F(\epsilon)}{d\epsilon d\Omega} = \int_0^{z_{max}} \frac{d^2 V}{dz d\Omega} dz \int_{L_{\gamma, min}}^{L_{\gamma, max}} \frac{dF_{\gamma}}{d\epsilon} \frac{dL_{\gamma}}{L_{\gamma} \ln(10)} \cdot \rho_{\gamma}(L_{\gamma}, z) \exp(-\tau_{\gamma, \gamma}(\epsilon, z)). \quad (5)$$

The minimum  $\gamma$ -ray luminosity value is set to  $10^{35}$  erg s $^{-1}$ , the maximum is set to  $10^{45}$  erg s $^{-1}$  and the maximum redshift is set to  $z_{max} = 5$ . These limits are wide enough to

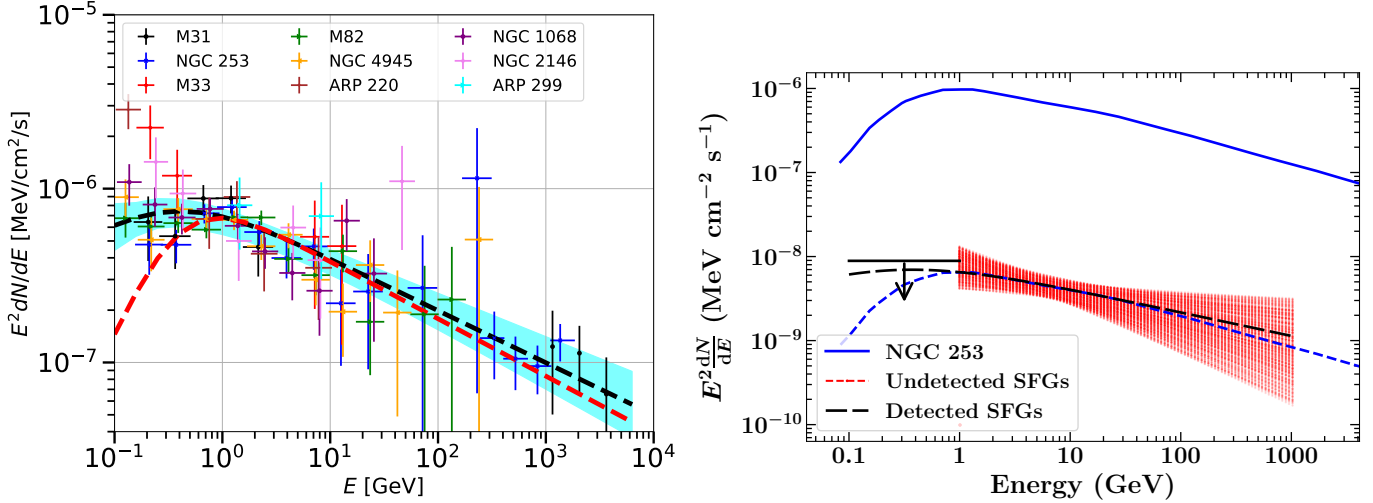


**Figure 8.** **Left Panel:** Composite SED model of resolved galaxies (black dashed line) with its  $1\sigma$  uncertainty band (cyan region). For clarity, the SED of each galaxy has scaled to a common value at  $t$  1 GeV and upper limits are not shown. The red-dashed line is the physical model fit to the LAT and H.E.S.S. data of NGC 253 (Abdalla et al. 2018). **Right Panel:** SED of unresolved galaxies (red hatched region and black 95 % C.L. upper limit) as determined from the stacking analysis of § 6.2 compared to the hadronic emission model (blue line) that reproduces the LAT and H.E.S.S. data of NGC 253 (Abdalla et al. 2018) rescaled (blue dashed line) to the SED of unresolved galaxies. The black dashed line shows the best-fit SED model of detected SFGs (see left panel).

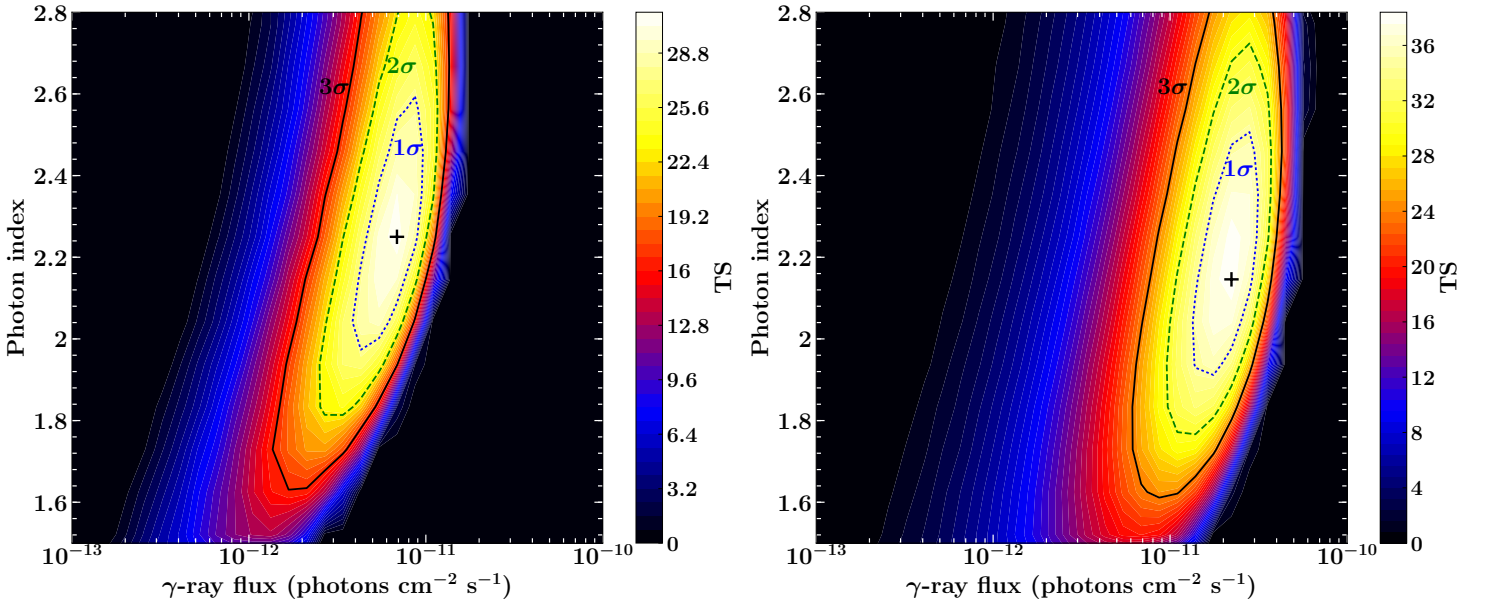


**Figure 9.** Detection significance as a function of photon index and  $\gamma$ -ray flux ( for energies above 1 GeV) for all 574 undetected galaxies (left) and for the 56 undetected galaxies in the Ackermann et al. (2012a) subsample (right).

contain the emission of the entire galaxy pop-

ulation. The quantity  $dF_\gamma/d\epsilon$  is the intrinsic

photon flux at energy  $\epsilon$ , for a source with a  $\gamma$ -ray luminosity  $L_\gamma$  and redshift  $z$ , and  $\rho_\gamma$  is the  $\gamma$ -ray luminosity function. High-energy  $\gamma$  rays ( $\epsilon > 20$  GeV) propagating in the Universe can be absorbed in interaction with the extragalactic background light (EBL) photons (e.g., Gould & Schröder 1966; Stecker et al. 1992; Finke et al. 2010), and  $\tau_{\gamma,\gamma}(\epsilon, z)$  is the optical depth for such process. In this study we adopt the attenuation model of Finke et al. (2010), which was found to be in good agreement with recent measurements of the EBL optical depth (Fermi-LAT Collaboration et al. 2018). The  $\gamma$ -ray absorption creates electron-positron pairs, which can inverse-Compton scatter off the cosmic microwave background photons, yielding secondary cascade emission at lower  $\gamma$ -ray energies. The cascade flux is, however, negligible because the SED of SFGs at high energy has a photon index greater than 2; for this reason we decide to neglect this contribution. We also do not consider the internal (to the source) absorption caused by a galaxy's interstellar radiation fields because it is important only above 10 TeV (Inoue 2011).

The  $\gamma$ -ray luminosity function is related to the IR one using:

$$\rho_\gamma(L_\gamma) = k\rho_{\text{IR}}(L_{\text{IR}}(L_\gamma)) \frac{d\log L_{\text{IR}}}{d\log L_\gamma}, \quad (6)$$

where  $k$  is assumed to be equal to 1 and the factor  $\frac{d\log L_{\text{IR}}}{d\log L_\gamma}$  is computed from the correlation between the  $\gamma$ -ray and IR luminosities reported in Sec. 5.2 for the combined analysis of detected and undetected sources in our sample. We consider the IR luminosity function provided by *Spitzer* observations of the VIMOS VLT Deep Survey and GOODS fields (Rodighiero et al. 2010). We also use the total IR luminosity function derived from the observations of the *Herschel* GTO PACS Evolutionary Probe Survey, in combination with the *HERschel* Multi-tiered Extragalactic Survey (HerMES) data (Gruppioni et al. 2013). Gruppioni et al. (2013) provide

the IR luminosity functions for normal spiral galaxies, starburst galaxies, and galaxies which contain an either obscured or low-luminosity AGN (SF-AGN). Finally they also report the IR luminosity function for galaxies containing a powerful starburst component, mainly responsible for their far-IR emission, and an AGN component that contributes significantly to the mid-IR (AGN1 and AGN2). In our calculation with the Gruppioni et al. (2013) IR luminosity function we include the spiral, starburst, and SF-AGN components.

Since  $\gamma$  rays and neutrinos are produced together in star-forming galaxies via the production and decay of energetic pions from hadronic CR interactions, the flux of  $\gamma$  rays and  $\nu$  (per flavor) are related as:

$$\Phi_\nu(E_\nu) = \frac{K_\pi}{4} \Phi_\gamma(E_\gamma), \quad (7)$$

where  $K_\pi$  is the relative charged-to-neutral pion rate. We assume for proton-gas ( $pp$ ) collisions  $K_\pi = 2$  which corresponds to an equal contribution of  $\pi^0$  and  $\pi^\pm$ . The average energies of  $\gamma$  rays and neutrinos are related as  $E_\gamma \approx 2E_\nu$ .

In Figure 10 we show the resulting prediction for the contribution of SFGs to the EGB and astrophysical  $\nu$  flux. SFGs on average contribute to the *Fermi*-LAT EGB at the level of 5% and to the IceCube  $\nu$  flux at the level of 3% (see also Bechtol et al. 2017; Sudoh et al. 2018). Our results for both the IR luminosity functions are compatible with the  $1\sigma$  upper limits for a non-blazar contribution to the EGB above 50 GeV derived in Ackermann et al. (2016). Finally, we note that the derived luminosity function underpredicts the current number of detected galaxies at  $\gamma$ -ray energies. This is due to the local overdensity, as most of our galaxies are detected within 50 Mpc. However, this does not affect our results, since the dominant contribution to the background flux comes from more distant galaxies.

## 8. CONCLUSIONS

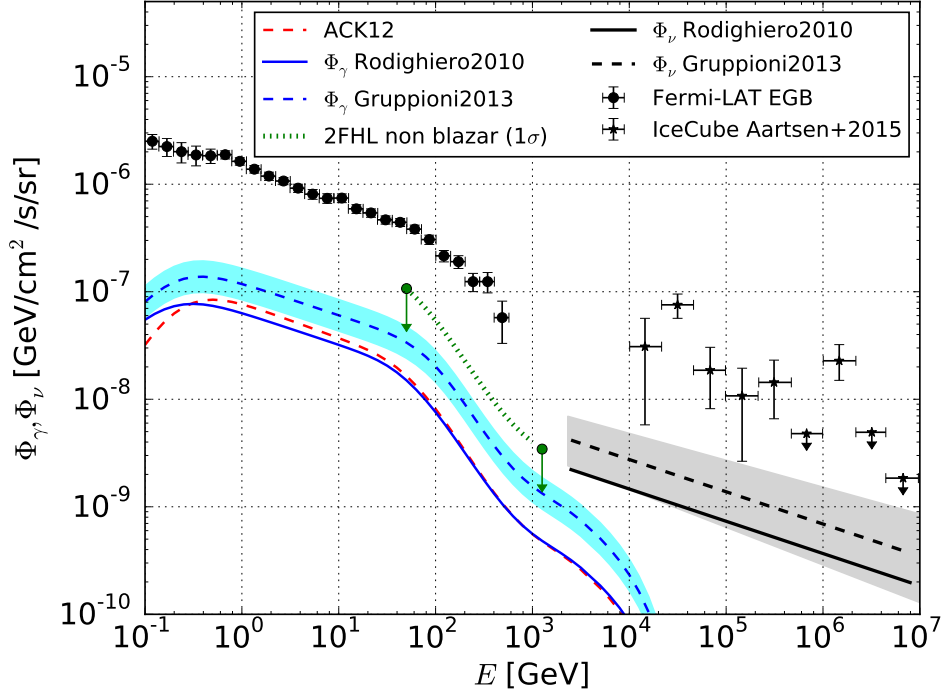


**Figure 10.** Gamma-ray intensity (blue solid line and cyan  $1\sigma$  band) and  $\nu$  (black solid line and gray  $1\sigma$  band) intensity from SFGs compared to the *Fermi*-LAT EGB (Ackermann et al. 2014) and astrophysical neutrino flux measured by IceCube (Aartsen et al. 2014). We also show the estimate for the SFG contribution to the EGB as derived in Ackermann et al. (2012a) (dashed red line). The dashed green line is the  $1\sigma$  upper limit for the non-blazar contribution to the EGB above 50 GeV (Ackermann et al. 2016).

We have used almost 10 years of *Fermi*-LAT data to characterize the  $\gamma$ -ray emission of SFGs and calculate their contribution to the *Fermi*-LAT EGB and IceCube  $\nu$  flux. Our findings are summarized as follows:

- We have reported the detection of 11 bona fide  $\gamma$ -ray emitting galaxies and 2 galaxy candidates, a sizable improvement over the 7 systems (not counting the Milky Way) reported in Ackermann et al. (2012a).
- Similarly to Linden (2017), we have shown that the emission of unresolved galaxies is detected by *Fermi*-LAT with a significance in the  $4.4 - 5.1\sigma$  range (assuming these objects can be characterized by an average flux and spectral index). This significance increases to  $7.2\sigma$  when unresolved galaxies are allowed to follow

the  $L_\gamma - L_{\text{IR}}$  correlation (see next bullet point).

- The  $\gamma$ -ray luminosity of both detected and unresolved galaxies has been found to correlate with the total IR luminosity, as in previous works (Ackermann et al. 2012a; Linden 2017). The significance of this correlation (using only the bona fide galaxies) is now near  $5\sigma$ .
- Using both detected and unresolved objects, we have constrained the average SED of  $\gamma$ -ray emitting galaxies, which was found (above 1 GeV) to be compatible with a power law with a photon index of  $\approx 2.2 - 2.3$ .
- Finally, we estimated that the contribution of star-forming galaxies to *Fermi*-LAT EGB and IceCube  $\nu$  flux is 5% and 3%, respectively. This scenario is



compatible with the current estimate for blazar and radio galaxy contributions to the EGB (see e.g. [Di Mauro et al. 2014](#); [Ajello et al. 2015](#); [Ackermann et al. 2016](#); [Di Mauro et al. 2018](#)).

MA acknowledges funding under NASA contract 80NSSC18K1718.

The *Fermi* LAT Collaboration acknowledges generous ongoing support from a number of agencies and institutes that have supported both the development and the operation of the LAT as well as scientific data analysis. These include the National Aeronautics and Space Administration and the Department of Energy in the United States, the Commissariat à l’Energie Atomique and the Centre National de la Recherche Scientifique / Institut National de Physique Nucléaire et de Physique des Particules in France, the Agenzia Spaziale Italiana and the Istituto Nazionale di

Fisica Nucleare in Italy, the Ministry of Education, Culture, Sports, Science and Technology (MEXT), High Energy Accelerator Research Organization (KEK) and Japan Aerospace Exploration Agency (JAXA) in Japan, and the K. A. Wallenberg Foundation, the Swedish Research Council and the Swedish National Space Board in Sweden. Additional support for science analysis during the operations phase is gratefully acknowledged from the Istituto Nazionale di Astrofisica in Italy and the Centre National d’Études Spatiales in France. This work performed in part under DOE Contract DE-AC02-76SF00515.

*Facility:* Fermi/LAT

## APPENDIX

### A. DETAILS FOR INDIVIDUAL GALAXIES

#### A.0.1. *Previously detected SFGs*

The brightest and closest SFGs detected by the LAT are the Large and Small Magellanic Clouds. They are detected as extended sources in *Fermi*-LAT data with extensions of about  $3.0^\circ$  and  $1.5^\circ$ , respectively. We consider for these two sources the spatial templates as given in the Preliminary 8 years list (FL8Y) (Ackermann et al. 2016).

Other bright SFGs detected in  $\gamma$  rays include M82 and NGC 253 (which are both at distance of 3.2 Mpc), NGC 4945 (at a distance of 4.0 Mpc), and NGC 1068 (at a distance of 10.6 Mpc). M82 is the largest galaxy of the M81 group in the Ursa Major constellation and it is the closest galaxy that hosts a starburst nucleus. Its star formation rate is about  $10 M_\odot \text{ yr}^{-1}$  and it has been detected at TeV energies by VERITAS (VERITAS Collaboration et al. 2009). NGC 253 is a giant barred spiral galaxy with a central starburst region. *NuSTAR* and *Chandra* observations pointed out the presence of X-ray sources but there is no clear evidence indicating that these sources are associated with a low-luminosity AGN (Lehmer et al. 2013). The star formation rate of NGC 253 has been estimated to be about  $5 M_\odot \text{ yr}^{-1}$  (Melo et al. 2002). NGC 253 has also been detected by H.E.S.S. at TeV energies with an SED given by a power law with index of 2.14 (Abramowski et al. 2012). NGC 4945 is a circumnuclear starburst galaxy that hosts an obscured Compton-thick Seyfert 2 nucleus that is among the brightest in the hard X-ray range (Yaqoob 2012). In Wojaczynski & Niedzwiecki (2017) the hint of a correlation between the  $\gamma$ -ray and X-ray emission has been reported, suggesting that the  $\gamma$ -ray emission may be associated with the Seyfert component. The lightcurve of this source (see § A.0.3 and Fig. 11) is particularly stable with no indications of variability. The apparent lack of  $\gamma$ -ray variability favors the interpretation of emission dominated by starburst processes. NGC 1068 is a source that exhibits both starburst and AGN activity, whose Seyfert 1 nucleus has been discovered in polarized light (Antonucci & Miller 1985). Models that explain the  $\gamma$ -ray emission from this source

also take into account the emission from the active nucleus (see, e.g., [Lenain et al. 2010](#); [Yoast-Hull et al. 2014](#); [Eichmann & Becker Tjus 2016](#)).

Among the faintest SFGs are M31, NGC 2146, and Arp 220 located at around 0.8 Mpc, 19.6 Mpc and 79.9 Mpc, respectively. M31 is the nearest massive spiral galaxy and it has a star formation rate of  $0.35\text{--}1.0 M_{\odot} \text{ yr}^{-1}$  ([Yin et al. 2009](#)). This source is found to be extended in our  $\gamma$ -ray analysis with a  $TS$  of extension of 21 and an angular size of  $0.45 \pm 0.10$  deg. The extension is modeled using a disk and yields a consistent morphology to what found in [Ackermann et al. \(2017\)](#). NGC 2146 is a starburst galaxy located at about 19.6 Mpc from Earth, whose starbursting episode is believed to have been started approximately 800 Myr ago when two galaxies collided (see [Greve et al. \(2006\)](#) and references therein). NGC 2146 shows no evidence of AGN activity in optical ([Ho et al. 1997](#)) or in mid-IR spectra ([Bernard-Salas et al. 2009](#)). This source exhibits a relatively high SFR of  $7.9 M_{\odot} \text{ yr}^{-1}$  ([Kennicutt et al. 2011](#)). Arp 220 is the farthest SFG detected by the LAT and it is a merger of two galaxies containing two dense nuclei separated by  $\sim 350$  pc (see, e.g., [Scoville et al. \(1998\)](#)). Both nuclei have high SFRs and dense molecular gas. This system has a total SFR of  $240 \pm 3.0 M_{\odot} \text{ yr}^{-1}$ , calculated from the far-IR luminosity ([Farrah et al. 2003](#)).

#### A.0.2. Newly detected SFGs

The newly detected SFGs are: M33 (see also [Karwin et al. 2019](#); [Di Mauro et al. 2019](#)), NGC 2403, UGC 11041, NGC 3424, and Arp 299. M33 is located roughly 870 kpc from Earth. It is a satellite galaxy of M31 and is the first extragalactic satellite to be detected in  $\gamma$  rays. M33 has a SFR in the range  $0.26\text{--}0.70 M_{\odot} \text{ yr}^{-1}$  ([Gardan et al. 2007](#)).

NGC 2403 is located at about 3.4 Mpc from Earth. It is an H I-dominated, low-mass spiral galaxy, and its HI gas disc extends beyond its optical disc ([Kang et al. 2017](#)). The total SFR has been measured to be about  $1.3 M_{\odot} \text{ yr}^{-1}$  ([Kennicutt et al. 2003](#)). Our analysis shows that the  $\gamma$ -ray peak is  $0.048^{\circ}$  away from the nominal center of the galaxy, with the 68% positional error of the source being  $0.036^{\circ}$ .

NGC 3424 is located at about 29 Mpc from Earth. It is considered to be a SFG ([Martínez-Galarza et al. 2016](#)) with a SFR of about  $4.5 M_{\odot} \text{ yr}^{-1}$ . In [Gavazzi et al. \(2011\)](#) the optical spectrum shows the presence of an AGN in the center of the Galaxy.

Arp 299 is located at a distance of 47.7 Mpc from Earth and it is an interacting system composed of two individual galaxies (IC 694 and NGC 36907) in an early dynamical stage. Powerful starburst regions with SFRs of about  $100 M_{\odot} \text{ yr}^{-1}$  have been identified in the system ([Alonso-Herrero et al. 2000](#)). Optical spectroscopic studies have classified IC 694 as starburst galaxy and NGC 3690 as starburst/LINER galaxy ([Coziol et al. 1998](#)), and mid-IR observations classified the system as starburst ([Laurent et al. 2000](#)). However, there are hints for the presence of AGN activity ([Della Ceca et al. 2002](#); [Ballo et al. 2004](#); [Gallais et al. 2004](#)).

#### A.0.3. Lightcurves of detected sources

In this section we report the details of the light curve analysis performed on the sample of SFGs. We use the function `gta.lightcurve` implemented in `Fermipy`. This function performs a fit to the ROI independently in each time bin. For each source `Fermipy` calculates the  $TS_{\text{var}}$ , which follows the definition provided in [Nolan et al. \(2012\)](#) as:

$$TS_{\text{var}} = \sum_i [\log L_i(F_i) - \log L_i(F_{\text{const}})], \quad (\text{A1})$$

where  $\log L_i(F_i)$  is the log-likelihood of the fit with the SED parameters of the source of interest free to vary in each  $i$ -th time bin, and  $\log L_i(F_{\text{const}})$  is the log-likelihood for the fit at the same time bin with the SED parameters fixed to provide the flux found in the entire time range. We add, as done in *Fermi*-LAT catalogs, a 2% systematic uncertainty to account for systematic errors in the calculation of the source exposure, resulting from small inaccuracies in the dependence of the IRFs on the source viewing angle, coupled with changes in the observing profile as the orbit of the spacecraft precesses. The results for the variability are reported in Table 2 as significance for the variability  $\sigma_{\text{var}}$ , calculated by converting  $TS_{\text{var}}$  to a significance by adopting the  $\chi^2$  distribution with 118 degrees of freedom for the six brightest sources and 38 degrees of freedom for the others. The lightcurves of all sources are shown in Figs. 11, 12, and 13.

The only significantly variable object is UGC 11041 with  $\sigma_{\text{var}} = 5.7$ . This source had a bright flare during the period 56500–56800 MJD. In this time range the source is detected with a  $TS = 76$  and has a best-fit position of  $RA(J2000) = 268.72^\circ \pm 0.07^\circ$  and  $DEC(J2000) = 34.76^\circ \pm 0.07^\circ$ , which is fully compatible with the galaxy’s known position. We also run the light-curve analysis for this source with a finer time bin of one month. This is shown in the right-hand panel of Figure 13 which demonstrates that the time scale for the flare is of about two months. The position of this source is coincident with the radio source NVSS J175451+344633. This indicates that the observed  $\gamma$ -ray emission is not due to star-formation activity, but rather points to the emission of a relativistic jet.

We test the accuracy of our lightcurve extraction method by analyzing pulsars, which are the least variable  $\gamma$ -ray sources on long timescales. We select pulsars from the 3FGL (Acero et al. 2015) with variability indices smaller than 55, detected at  $|b| > 4^\circ$ , at least  $20^\circ$  away from the Galactic center, and with a statistical significance greater than  $8\sigma$ . This leaves us with 50 pulsars on which we run our variability analysis using one time interval per month. We find that these pulsars have an average  $TS_{\text{var}}$  of 110, which implies  $\sim 0.40\sigma$  significance for the variability. The mean and standard deviation for the  $TS_{\text{var}}$  distribution are 110 and 45, respectively. Therefore, all the results for our SFGs, except for UGC 11041, are consistent with the results found for our sample of pulsars. The most-variable pulsars in our sample are the following: PSR J1836+5925 ( $\sigma_{\text{var}} = 6.2\sigma$ ), PSR J1231–1411 ( $\sigma_{\text{var}} = 5.6\sigma$ ), PSR J1057–5226 ( $\sigma_{\text{var}} = 4.8\sigma$ ), PSR J0218+4232 ( $\sigma_{\text{var}} = 4.7\sigma$ ), PSR J1311–3430 ( $\sigma_{\text{var}} = 4.2\sigma$ ) and PSR J0357+3205 ( $\sigma_{\text{var}} = 4.0\sigma$ ).

Finally, we produce lightcurves for the brightest SFGs using the adaptive binning method of Lott et al. (2012). In this method, the time bins have been optimized to have a fractional uncertainty of 15% for all sources except NGC 1068 and M31, for which a fractional uncertainty of 20% was used. The lightcurves, reported in Figures 15 and 16, confirm the overall result of the lack of variability for our sample of galaxies.

## B. VALIDATION OF THE STACKING TECHNIQUE

In order to be able to interpret correctly the results of the stacking analysis we performed a test where we simulated 10 years of Pass 8 data for 20 sources at  $|b| > 10^\circ$ , whose spectra are modeled using a power law. The power-law indices are extracted from a Gaussian distribution with a mean of 2.2 and a dispersion of 0.2, while the fluxes are extracted from a power-law distribution with index  $-2.5$  having an average of  $6.41 \times 10^{-10}$  ph cm $^{-2}$  s $^{-1}$ . The simulations include the diffuse (Galactic and isotropic) emission as well as all the point sources from the FL8Y. A stacking analysis was performed for the simulated dataset as described in § 3.2, and the results are presented in Figure 17. The average emission of these simulated sources is detected with a  $TS \approx 32$ . The best-fit photon

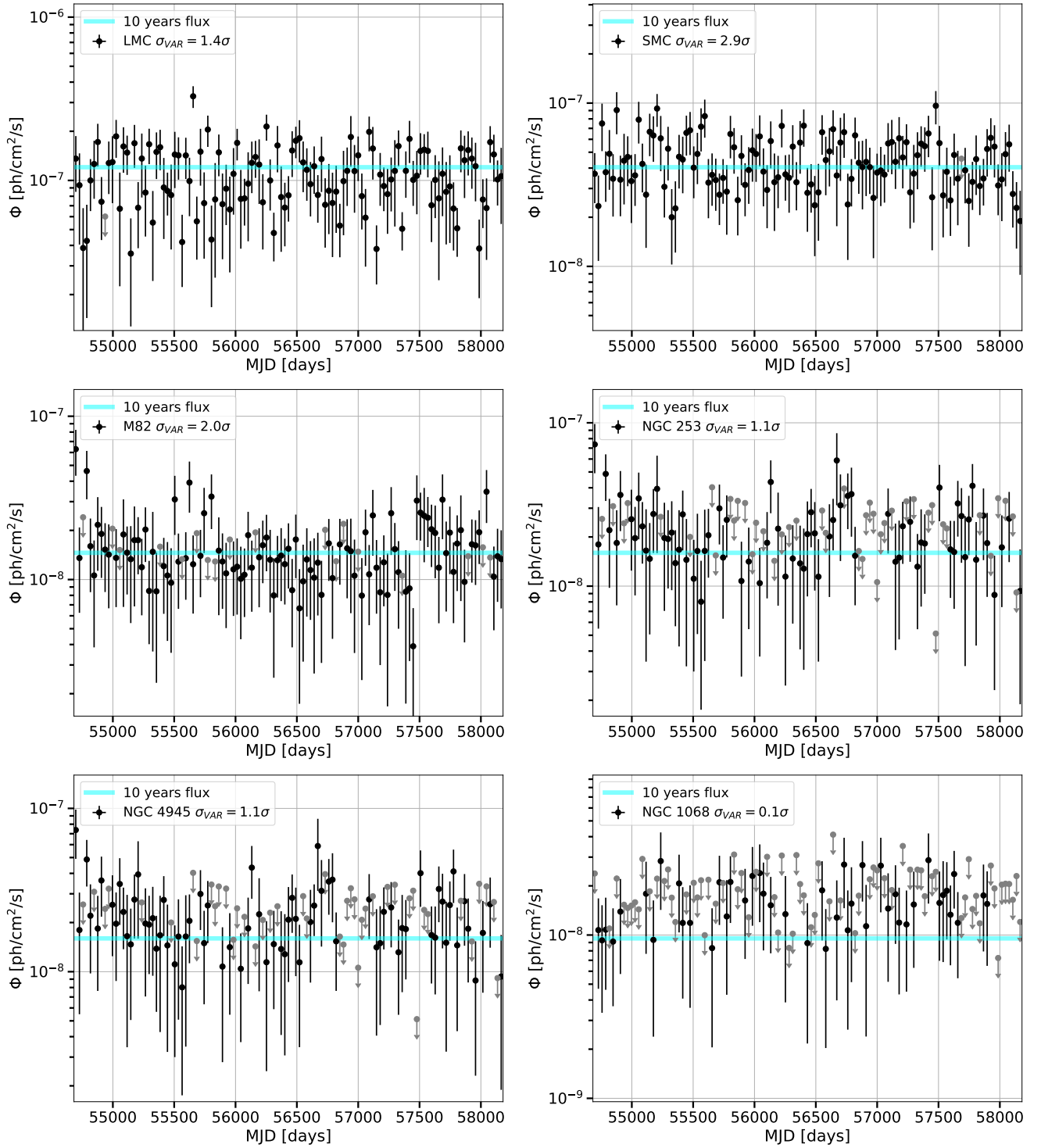


**Figure 11.** Light curves for the SFGs detected in our sample. The black data show the flux in each time bin and the cyan lines indicate the fluxes measured in the full dataset. The gray downward arrows are  $1\sigma$  upper limits to the source flux computed when the source  $TS < 6$ .

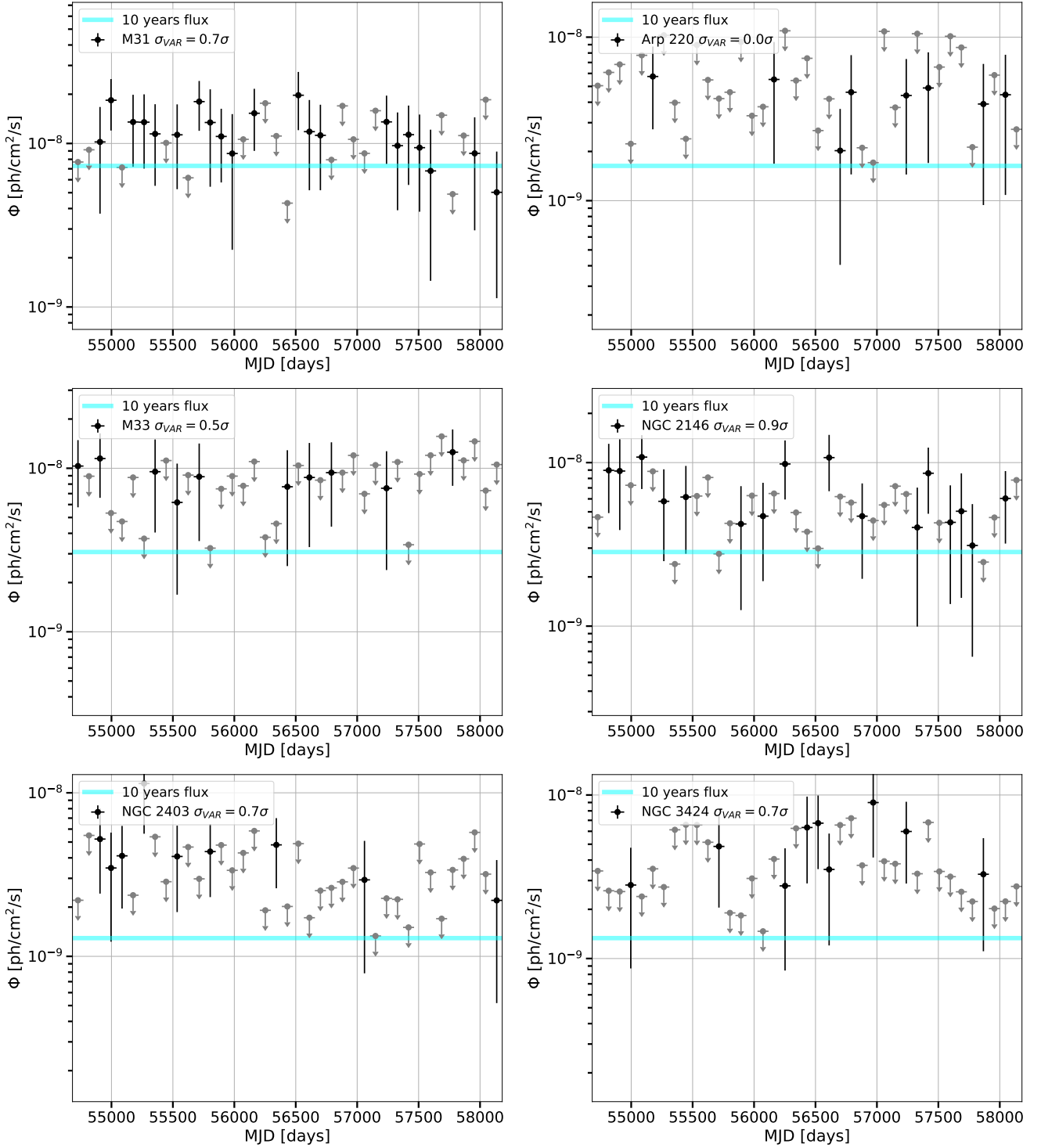


**Figure 12.** Same as in Figure 11.

index and flux are  $2.12 \pm 0.12$  and  $5.0 \pm 2.0 \times 10^{-10} \text{ ph cm}^{-2} \text{ s}^{-1}$ , respectively, which is in agreement with the average values of the simulated sources. From this analysis we conclude that the stacking analysis provides a measurement of the average properties (in this case photon index and flux) of the unresolved population.

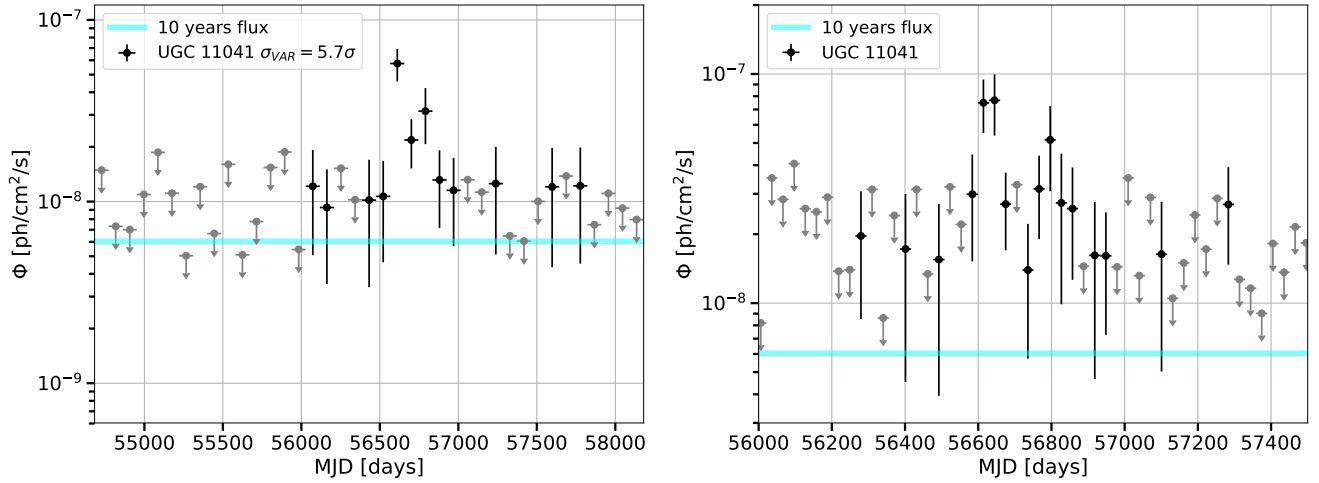


**Figure 13.** Same as in Figure 11.

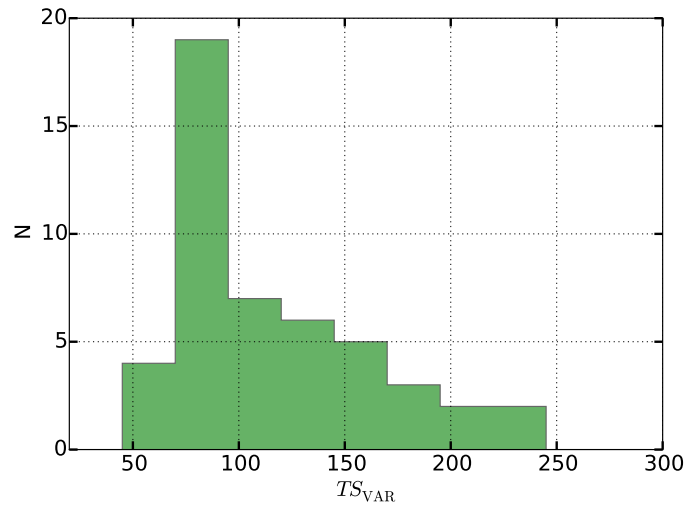


**Figure 14.** Histogram of the  $TS_{\text{var}}$  for the 50 selected pulsars in our sample.

## REFERENCES

- Aartsen, M. G., Ackermann, M., Adams, J., et al. 2014, *Phys. Rev. Lett.*, 113, 101101
- Aartsen, M. G., Abbasi, R., Abdou, Y., et al. 2013, *Physical Review Letters*, 111, 021103
- Aartsen, M. G., Abraham, K., Ackermann, M., et al. 2015, *ApJ*, 809, 98
- Aartsen, M. G., Ackermann, M., Adams, J., et al. 2017a, *ApJ*, 849, 67
- Aartsen, M. G., Abraham, K., Ackermann, M., et al. 2017b, *ApJ*, 835, 45
- Abdalla, H., et al. 2018, *Astron. Astrophys.*, 617, A73
- Abdalla, H., Aharonian, F., Ait Benkhali, F., et al. 2018, *A&A*, 617, A73
- Abramowski, A., Acero, F., Aharonian, F., et al. 2012, *ApJ*, 757, 158
- Acero, F., Ackermann, M., Ajello, M., et al. 2015, *ApJS*, 218, 23
- Acero, F., et al. 2016, *Astrophys. J. Suppl.*, 223, 26
- Ackermann, M., Ajello, M., Allafort, A., et al. 2012a, *ApJ*, 755, 164
- . 2012b, *ApJ*, 747, 104
- Ackermann, M., Ajello, M., Albert, A., et al. 2014, arXiv:1410.3696, arXiv:1410.3696:1410.3696

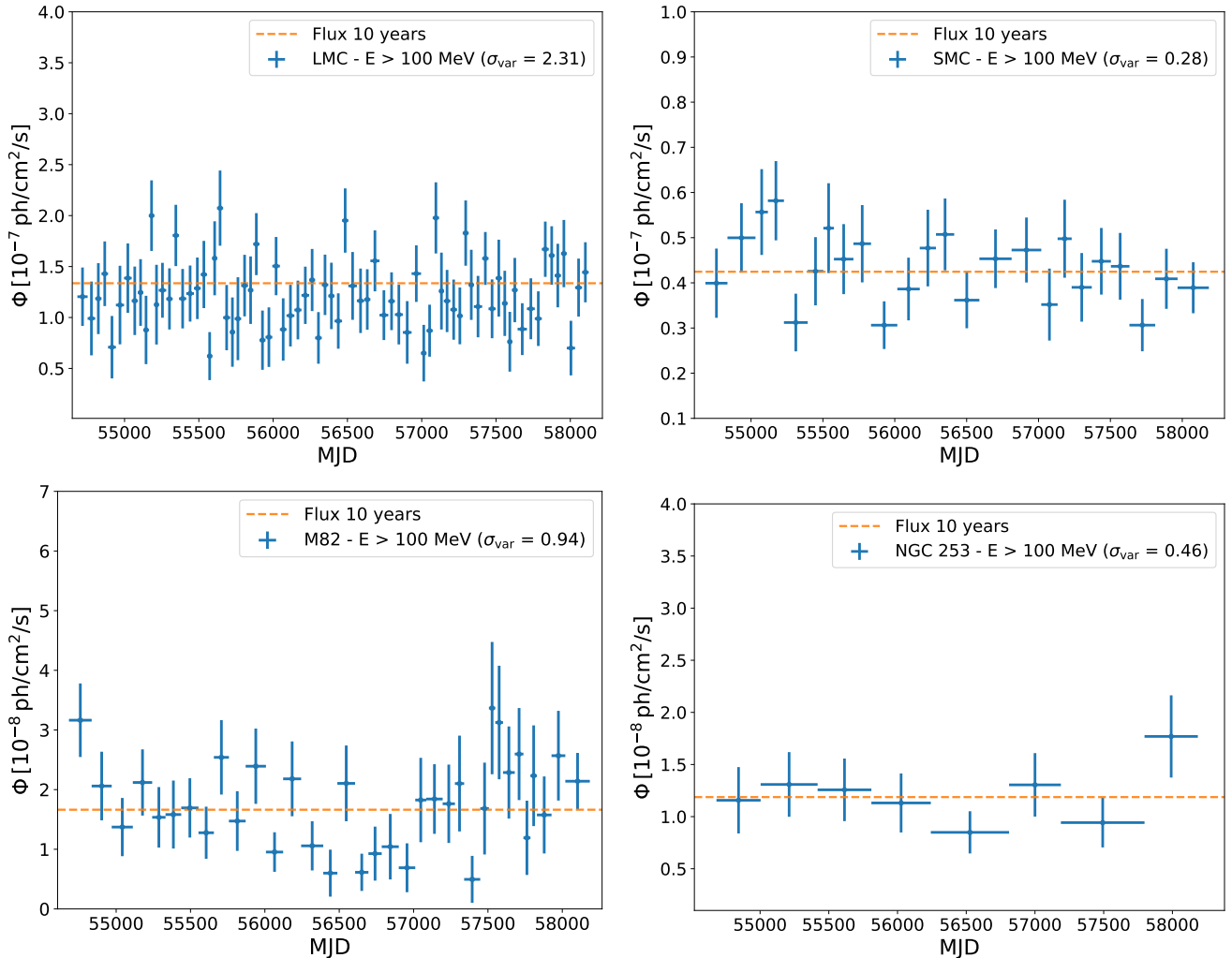


**Figure 15.** Constant signal-to-noise ratio light curves of the brightest galaxies.

- Ackermann, M., et al. 2016, *Astron. Astrophys.*, 586, A71
- Ackermann, M., Ajello, M., Albert, A., et al. 2016, *Physical Review Letters*, 116, 151105
- Ackermann, M., et al. 2017, *Astrophys. J.*, 836, 208
- Adamo, A., Smith, L. J., Gallagher, J. S., et al. 2012, *MNRAS*, 426, 1185
- Aharonian, F., Akhperjanian, A. G., Bazer-Bachi, A. R., et al. 2005, *A&A*, 442, 177
- Ahlers, M., & Halzen, F. 2014, *PhRvD*, 90, 043005
- Ajello, M., Gasparrini, D., Sánchez-Conde, M., et al. 2015, *ApJL*, 800, L27
- Akritas, M. G., & Siebert, J. 1996, *MNRAS*, 278, 919
- Alonso-Herrero, A., Rieke, G. H., Rieke, M. J., & Scoville, N. Z. 2000, *ApJ*, 532, 845
- Antonucci, R. R. J., & Miller, J. S. 1985, *ApJ*, 297, 621
- Ballo, L., Braito, V., Della Ceca, R., et al. 2004, *ApJ*, 600, 634
- Bechtol, K., Ahlers, M., Di Mauro, M., Ajello, M., & Vandenbroucke, J. 2017, *ApJ*, 836, 47
- Bechtol, K., Ahlers, M., Mauro, M. D., Ajello, M., & Vandenbroucke, J. 2017, *ApJ*, 836, 47
- Bernard-Salas, J., Spoon, H. W. W., Charmandaris, V., et al. 2009, *ApJS*, 184, 230
- Coziol, R., Torres, C. A. O., Quast, G. R., Contini, T., & Davoust, E. 1998, *ApJS*, 119, 239
- Della Ceca, R., Ballo, L., Tavecchio, F., et al. 2002, *ApJL*, 581, L9
- Di Mauro, M., Calore, F., Donato, F., Ajello, M., & Latronico, L. 2013, *ApJ*, 780, 161
- Di Mauro, M., & Donato. 2014, in prep.



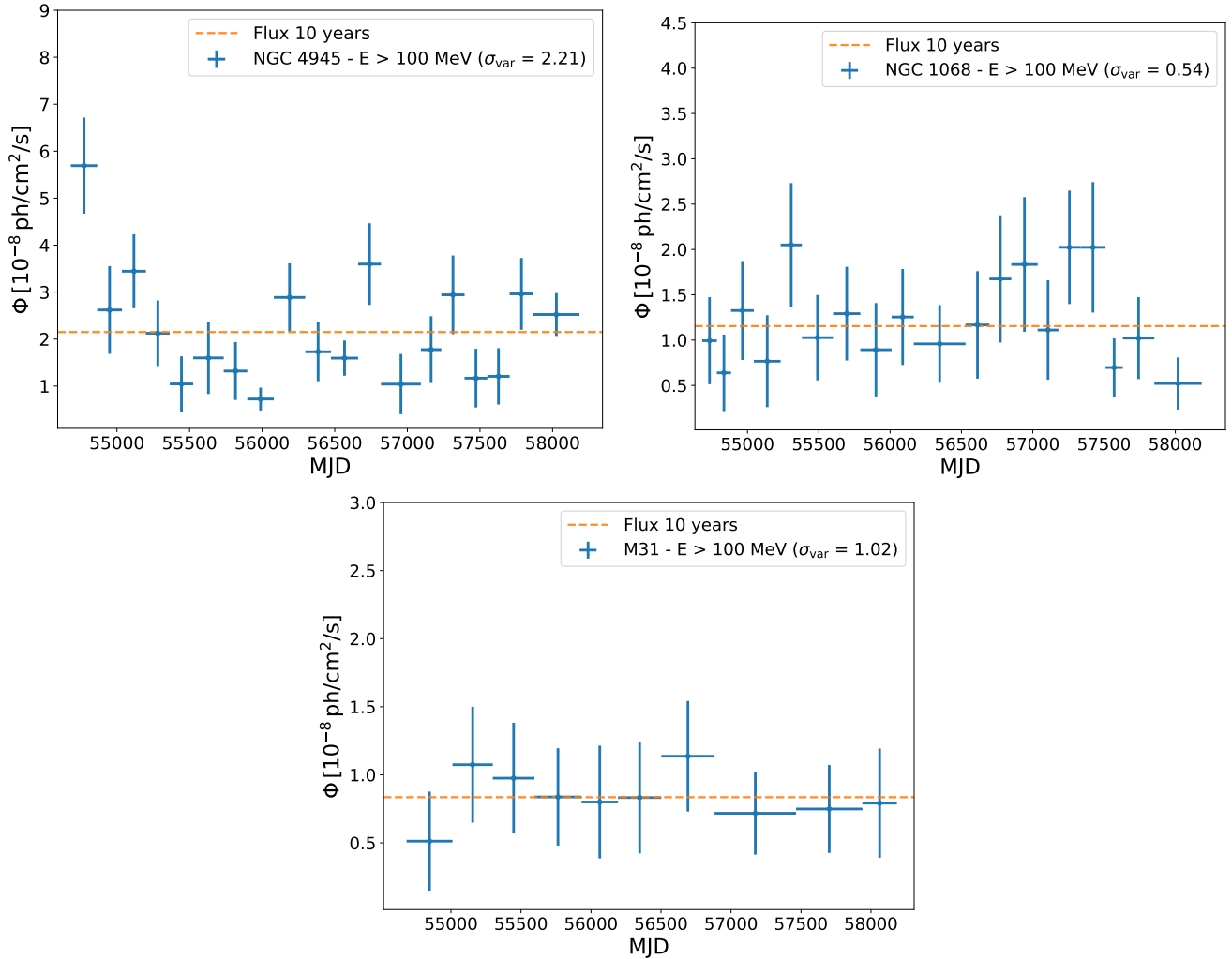


**Figure 16.** Same as in Figure 15.

- Di Mauro, M., Donato, F., Lamanna, G., Sanchez, D. A., & Serpico, P. D. 2014, *Astrophys. J.*, 786, 129
- Di Mauro, M., Hou, X., Eckner, C., Zaharijas, G., & Charles, E. 2019, *Physical Review D*, 99, 110
- Di Mauro, M., Manconi, S., Zechlin, H.-S., et al. 2018, *ApJ*, 856, 106
- Eichmann, B., & Becker Tjus, J. 2016, *ApJ*, 821, 87
- Farrah, D., Afonso, J., Efstathiou, A., et al. 2003, *MNRAS*, 343, 585
- Fermi-LAT Collaboration, Abdollahi, S., Ackermann, M., et al. 2018, *Science*, 362, 1031
- Finke, J. D., Razzaque, S., & Dermer, C. D. 2010, *ApJ*, 712, 238
- Freedman, W. L., Madore, B. F., Gibson, B. K., et al. 2001, *ApJ*, 553, 47
- Gallais, P., Charmandaris, V., Le Floc'h, E., et al. 2004, *A&A*, 414, 845
- Gao, Y., & Solomon, P. M. 2004, *ApJ*, 606, 271
- Gardan, E., Braine, J., Schuster, K. F., Brouillet, N., & Sievers, A. 2007, *A&A*, 473, 91
- Gavazzi, G., Savorgnan, G., & Fumagalli, Mattia. 2011, *A&A*, 534, A31
- Gould, R. J., & Schröder, G. 1966, *Physical Review Letters*, 16, 252
- Greve, Neining, N., Sievers, A., & Tarchi, A. 2006, *A&A*, 459, 441
- Gruppioni, C., et al. 2013, *Mon. Not. Roy. Astron. Soc.*, 432, 23
- Hayashida, M., Stawarz, L., Cheung, C. C., et al. 2013, *ApJ*, 779, 131
- Ho, L. C., Filippenko, A. V., & Sargent, W. L. W. 1997, *ApJS*, 112, 315

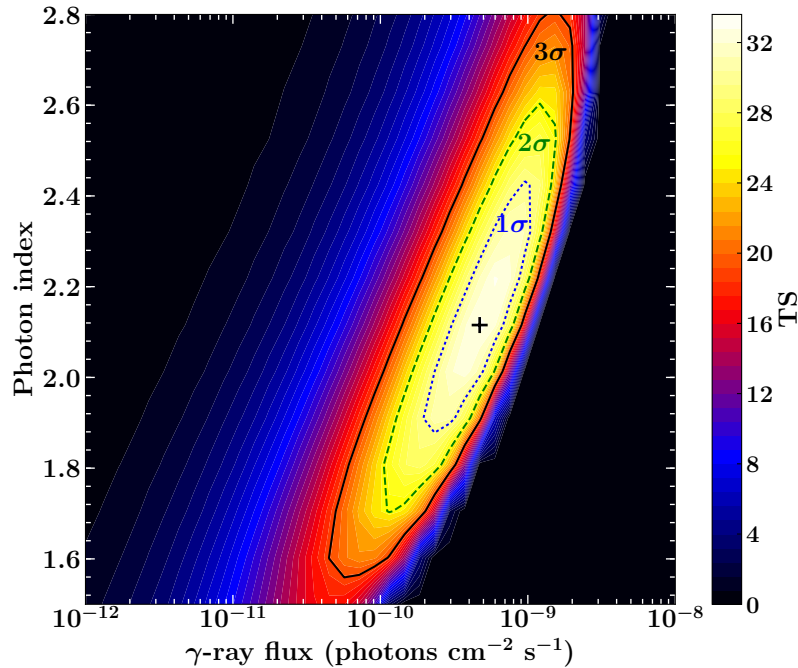


**Figure 17.** Stack of 20 simulated sources with average photon index of  $2.2 \pm 0.2$  and average (100 MeV – 800 GeV) flux of  $6.1(\pm 1.8) \times 10^{-10}$  ph cm $^{-2}$  s $^{-1}$

- IceCube Collaboration, Aartsen, M. G., Ackermann, M., et al. 2018, *Science*, 361, eaat1378
- Inoue, Y. 2011, *ApJ*, 728, 11
- Kang, X., Zhang, F., & Chang, R. 2017, *MNRAS*, 469, 1636
- Karwin, C. M., Murgia, S., Campbell, S., & Moskalenko, I. V. 2019, *ApJ*, 880, 95
- Kennicutt, R. C., Calzetti, D., Aniano, G., et al. 2011, *PASP*, 123, 1347
- Kennicutt, Jr., R. C., Armus, L., Bendo, G., et al. 2003, *PASP*, 115, 928
- Kraushaar, W. L., Clark, G. W., Garmire, G. P., et al. 1973, *ApJ*, 186, 401
- Laurent, O., Mirabel, I. F., Charmandaris, V., et al. 2000, *A&A*, 359, 887
- Lehmer, B. D., Wik, D. R., Hornschemeier, A. E., et al. 2013, *ApJ*, 771, 134
- Lenain, J. P., Ricci, C., Türler, M., Dorner, D., & Walter, R. 2010, *A&A*, 524, A72
- Linden, T. 2017, *Physical Review D*, 96, 453
- Lott, B., Escande, L., Larsson, S., & Ballet, J. 2012, *A&A*, 544, A6
- Martínez-Galarza, J. R., Smith, H. A., Lanz, L., et al. 2016, *ApJ*, 817, 76
- Massaro, E., Maselli, A., Leto, C., et al. 2015, *Ap&SS*, 357, 75
- Mattox, J. R., Bertsch, D. L., Chiang, J., et al. 1996, *ApJ*, 461, 396
- Melo, V. P., Pérez García, A. M., Acosta-Pulido, J. A., Muñoz-Tuñón, C., & Rodríguez Espinosa, J. M. 2002, *ApJ*, 574, 709
- Mouhcine, M., Ferguson, H. C., Rich, R. M., Brown, T. M., & Smith, T. E. 2005, *ApJ*, 633, 810
- Mould, J., & Sakai, S. 2008, *ApJL*, 686, L75
- Murase, K., & Waxman, E. 2016, *PhRvD*, 94, 103006
- Nasonova, O. G., de Freitas Pacheco, J. A., & Karachentsev, I. D. 2011, *A&A*, 532, A104
- Nolan, P. L., Abdo, A. A., Ackermann, M., et al. 2012, *ApJS*, 199, 31
- Paliya, V. S., Domínguez, A., Ajello, M., Franckowiak, A., & Hartmann, D. 2019, *The Astrophysical Journal*, 882, L3
- Peng, F.-K., & Wang, X.-Y. 2017, *The Astrophysical Journal*, 835, 269
- Peng, F.-K., Wang, X.-Y., Liu, R.-Y., Tang, Q.-W., & Wang, J.-F. 2016, *The Astrophysical Journal Letters*, 821, L20

- Peng, F.-K., Zhang, H.-M., Wang, X.-Y., Wang, J.-F., & Zhi, Q.-J. 2019, *The Astrophysical Journal*, 884, 91
- Rodighiero, G., Vaccari, M., Franceschini, A., et al. 2010, *A&A*, 515, A8+
- Sanders, D. B., Mazzarella, J. M., Kim, D. C., Surace, J. A., & Soifer, B. T. 2003, *Astron. J.*, 126, 1607
- Sanders, D. B., & Mirabel, I. F. 1996, *ARA&A*, 34, 749
- Scoville, N. Z., Evans, A. S., Dinshaw, N., et al. 1998, *ApJL*, 492, L107
- Stecker, F. W., de Jager, O. C., & Salamon, M. H. 1992, *ApJL*, 390, L49
- Sudoh, T., Totani, T., & Kawanaka, N. 2018, *PASJ*, 70, 49
- Tang, Q.-W., Wang, X.-Y., & Thomas Tam, P.-H. 2014, *Astrophys. J.*, 794, 26
- The Fermi-LAT collaboration. 2019, arXiv:1902.10045, arXiv:1902.10045
- Theureau, G., Hanski, M. O., Coudreau, N., Hallet, N., & Martin, J. M. 2007, *A&A*, 465, 71
- Tully, R. B., Courtois, H. M., Dolphin, A. E., et al. 2013, *AJ*, 146, 86
- Vacca, W. D., Hamilton, R. T., Savage, M., et al. 2015, *ApJ*, 804, 66
- VERITAS Collaboration, Acciari, V. A., Aliu, E., et al. 2009, *Nature*, 462, 770
- Wojaczynski, R., & Niedzwiecki, A. 2017, *Astrophys. J.*, 849, 97
- Wood, M., Caputo, R., Charles, E., et al. 2017, ArXiv e-prints, arXiv:1707.09551
- Wu, W., Clayton, G. C., Gordon, K. D., et al. 2002, *ApJS*, 143, 377
- Xi, S.-Q., Liu, R.-Y., Wang, X.-Y., et al. 2020, arXiv e-prints, arXiv:2003.04795
- Yaqoob, T. 2012, *MNRAS*, 423, 3360
- Yin, J., Hou, J. L., Prantzos, N., et al. 2009, *A&A*, 505, 497
- Yoast-Hull, T. M., Gallagher, III, J. S., Zweibel, E. G., & Everett, J. E. 2014, *ApJ*, 780, 137